



**NUCLEAR STRUCTURE OF RHENIUM-186 REVEALED BY NEUTRON-
CAPTURE GAMMA RAYS**

THESIS

Andrew G. Lerch, Captain, USA

AFIT-ENP-14-M-21

**DEPARTMENT OF THE AIR FORCE
AIR UNIVERSITY**

AIR FORCE INSTITUTE OF TECHNOLOGY

Wright-Patterson Air Force Base, Ohio

DISTRIBUTION STATEMENT A.
APPROVED FOR PUBLIC RELEASE; DISTRIBUTION UNLIMITED.

The views expressed in this thesis are those of the author and do not reflect the official policy or position of the United States Air Force, Department of Defense, or the United States Government. This material is declared a work of the U.S. Government and is not subject to copyright protection in the United States.

AFIT-ENP-14-M-21

NUCLEAR STRUCTURE OF RHENIUM-186 REVEALED BY NEUTRON-
CAPTURE GAMMA RAYS

THESIS

Presented to the Faculty

Department of Engineering Physics

Graduate School of Engineering and Management

Air Force Institute of Technology

Air University

Air Education and Training Command

In Partial Fulfillment of the Requirements for the

Degree of Master of Science

Andrew G. Lerch, BS

Captain, USA

March 2014

DISTRIBUTION STATEMENT A.
APPROVED FOR PUBLIC RELEASE; DISTRIBUTION UNLIMITED.

NUCLEAR STRUCTURE OF RHENIUM-186 REVEALED BY NEUTRON-
CAPTURE GAMMA RAYS

Andrew G. Lerch, BS

Captain, USA

Approved:

//signed//
LTC Stephen R. McHale (Chairman)

3/11/2014
Date

//signed//
John W. McClory, Ph. D. (Member)

3/17/2014
Date

//signed//
James J. Carroll, Ph. D. (Member)

3/6/2014
Date

//signed//
Aaron M. Hurst, Ph. D. (Member)

2/24/2014
Date

Abstract

The total radiative thermal neutron-capture cross section of $^{185}\text{Re}(n,\gamma)$ was calculated from measurements of its gamma-ray spectrum following irradiation of a highly enriched ^{185}Re target in the guided thermal-neutron beam at the Budapest Research Reactor. The cross section was obtained by first summing the experimentally measured partial gamma ray-production cross sections associated with the known ground-state transitions below 323 keV. Combined with the contribution to ground-state population from the quasi-continuum, which was generated by the DICEBOX statistical-decay code, the resulting thermal neutron-capture cross section was determined to be 84(6) b. This result is statistically comparable to previous works. Additionally, 12 levels and 54 primary transitions were newly identified in this work via the binding-energy test, thus improving the decay scheme. All observed primary transitions populating levels below 865 keV were used to perform an independent measurement of the neutron-separation energy, which was found to be 6179.45(30) keV. This result is also consistent with measurements made in previous works and with the adopted neutron-separation energy of 6179.7(7) keV.

To Esther, Sofia, and Sebastian

Acknowledgments

I would like to express my gratitude to LTC Stephen R. McHale and Dr. John W. McClory for their confidence in me, the autonomy they granted to me, and their support throughout the course of this research effort. I would also like to extend my deep appreciation to Dr. James J. Carroll of the U.S. Army Research Laboratory for giving me the opportunity to work on this project, in addition to the time and effort he spent providing me with mentorship and instruction. Furthermore, the conduct of this research would not have been possible without the diligent guidance and considerable expertise provided by Dr. Aaron M. Hurst of Lawrence Berkeley National Laboratory. I am also very grateful for the technical advice offered by Dr. László Szentmiklósi of the Hungarian Academy of Sciences' Centre for Energy Research. The original experiment was supported by Defense Threat Reduction Agency (DTRA) grant HDTRA1-08-0014 through Youngstown State University. Ben Detwiler of Youngstown State University assisted Dr. Carroll with data acquisition.

Andrew G. Lerch

Table of Contents

	Page
Abstract	iv
Acknowledgments.....	vi
Table of Contents	vii
List of Figures	ix
List of Tables	x
I. Introduction	1
1.1 Motivation	1
1.2 Background	2
1.3 Problem	3
1.4 Hypothesis	3
1.5 Scope	3
1.6 Approach	4
II. Theory	7
2.1 Nuclear Models	7
2.2 Compound Nucleus Formation via Thermal-neutron Capture.....	14
2.3 Gamma-ray Decay and Internal Conversion	16
2.3.1 Gamma-ray Decay	16
2.3.2 Internal Conversion	25
2.4 Statistical Gamma Analysis	26
2.4.1 Level Density Models	28
2.4.2 Photon Strength Functions	30
III. Experimental Setup and Data Analysis Methodology	35
3.1 Experimental Setup	35
3.2 Data Analysis Methodology.....	40
IV. Results and Discussion	45
4.1 Nonlinearity Correction and Efficiency Calibration	45
4.1.1 Nonlinearity Correction.....	46
4.1.2 Efficiency Calibration	47
4.2 High-energy (n, γ) Spectrum.....	48
4.3 Low-energy (n, γ) Spectrum	54

4.4 Statistical Model Calculations.....	61
4.5 Energy Levels of Interest	65
4.5.1 1^- Ground State.....	65
4.5.2 2^- Level at 59 keV	65
4.5.3 3^- Level at 99 keV	66
4.5.4 3^- Level at 146 keV	67
4.5.5 8^+ Level at 149 keV	67
4.5.6 4^- Level at 174 keV	68
4.5.7 6^- Level at 186 keV	68
4.5.8 2^- Level at 211 keV	69
4.5.9 4^- Level at 269 keV	69
4.5.10 4^- Level at 274 keV	70
4.5.11 3^+ Level at 314 keV	70
4.5.12 1^- Level at 316 keV	71
4.5.13 5^- Level at 318 keV	71
4.5.14 3^- Level at 322 keV	72
4.5.15 5^+ Level at 330 keV	72
4.5.16 3^+ Level at 351 keV	73
4.5.17 2^- Level at 378 keV	73
4.5.18 5^- Level at 418 keV	73
4.5.19 4^+ Level at 420 keV	74
4.5.20 Summary of Energy Level Measurements	74
4.6 Neutron Separation Energy for ^{185}Re	75
4.7 Thermal Neutron-capture Cross Section for $^{185}\text{Re}(n,\gamma)$	78
V. Conclusions and Recommendations	81
5.1 Conclusions of Research	81
5.2 Significance of Research.....	81
5.3 Recommendations for Future Research	82
Appendix A.....	83
Appendix B	84
Bibliography	95
Vita.....	100

List of Figures

Figure	Page
1. Single-particle orbits for both prolate and oblate deformations	9
2. Possible values of Ω at various orientations	10
3. Theoretical energy level configuration of ^{186}Re	12
4. Nilsson configuration of ^{186}Re states for the metastable-excited state	13
5. Total cross section of ^{185}Re	16
6. Electromagnetic fields generated by electric and magnetic dipoles	20
7. Illustration of giant resonance modes	33
8. The PGAA and NIPS facilities	35
9. The 10 MW _t Budapest Research Reactor.	36
10. The PGAA target station and Compton-suppressed HPGe detector.	38
11. Diagram of the PGAA facility <i>n</i> -type HPGe detector	38
12. Preparation of the enriched ^{185}Re metal powder target.....	39
13. Flow chart of the data analysis procedure.....	40
14. Inspection of peaks within a region for goodness of fit.....	41
15. Hypermet-PC nonlinearity in channel correction	46
16. Hypermet-PC detector efficiency correction.	47
17. An example of the binding energy test	49
18. Population and depopulation of various energy levels	55
19. Comparison of various combinations of LD models and GDER PSF	64

List of Tables

Table	Page
1. Elemental comparator cross sections used in the standardization procedure	42
2. Observed primary transitions in the ^{186}Re high-energy spectrum.	51
3. The low-energy region decay scheme of ^{186}Re	56
4. Level relative intensity comparison for the first 15 excited states.....	59
5. Level absolute intensity comparison for the first 15 excited states	61
6. Level density parameters	62
7. Lorentz GDER and GQER resonance parameters	62
8. Summary of energy level measurements	74
9. Neutron separation energy calculated with the ENSDF-adopted levels	76
10. Neutron separation energy calculated with the experimental levels.....	77
11. Summary of S_n measurements	78
12. Partial gamma ray-production cross sections for ground state transitions	79
13. Summary of σ_0 measurements.....	79

NUCLEAR STRUCTURE OF RHENIUM-186 REVEALED BY NEUTRON-CAPTURE GAMMA RAYS

I. Introduction

1.1 Motivation

The ^{186}Re isotope possesses a metastable-excited state that has a half-life of 200,000 years and it is approximately situated at 149 keV above the nuclear ground state [1]. If depletion of this isomer is achieved with incident energy sufficiently less than that generated by its subsequent transitions from an intermediate level to the ground state, then prompt energy can be generated for every isomer depleted. This depletion is one case where the potential exists for use in on-demand, high-energy density applications. What is more, the ground state of ^{186}Re has a half-life of 3.7 days, from which it decays via β^- emission with a branching ratio of 92.5%, releasing electrons with energies as high as 1.07 MeV [2]. As a result, there is a potential to generate both prompt energy from the depletion of the isomeric state and delayed energy from the subsequent ground-state decay.

A direct depletion experiment will be required to test the suitability of ^{186}Re for power production applications, such as a radioisotope battery. Although it did not specifically mention nuclear isomers, the U.S. Department of Defense Science Board's October 2013 report recommended that \$25 million be committed to the technological development of such a power source [3]. To date, the nuclear structure of ^{186}Re remains uncertain. An enhanced understanding of its structure is required in order to set the conditions for a depletion experiment. This work examines the de-excitation of ^{186}Re

resulting from thermal-neutron capture, which will provide new experimental information about the isotope's various energy levels and transitions, also known as its de-excitation decay scheme.

1.2 Background

Nuclear isomeric states or isomers are long-lived excited states of nuclei. Isomer half-lives generally range from nanoseconds all the way up to 10^{15} years, whereas half-lives of typical gamma-ray decays are on the order of picoseconds or less. If the isomer possesses significant longevity, meaning more than one millisecond, it is categorized as metastable and is denoted by the superscript “m”. For example, the customary notation of the rhenium-186 isomer is $^{186\text{m}}\text{Re}$. Some nuclei possess more than one metastable state in which case the “m” is followed by a number indicating its position in ascending order of excitation energy [4]. An instance of this occurs with the holmium-160 isotope, which possesses two metastable states: $^{160\text{m1}}\text{Ho}$ at 60 keV and $^{160\text{m2}}\text{Ho}$ at 169 keV with half-lives of approximately five hours and three seconds, respectively [2].

Isomers are important in nuclear physics and astrophysics, but have also found application in medical imaging. In conjunction with another compound, $^{99\text{m}}\text{Tc}$ is used to image the human body. The other compound seeks out enflamed regions of tissue and the attached $^{99\text{m}}\text{Tc}$ emits soft gamma rays that are subsequently captured by a gamma-ray camera. Moreover, its half-life of six hours is a near ideal duration for the purposes of this medical procedure [4]. Isomers are also used in studying the makeup of the universe. In particular, they provide understanding of the early and present isotopic constituency of the planet. The unique combination of a long half-life and high excitation energy

make some isomers of interest for an even more significant application, on-demand energy generation [4, 5].

1.3 Problem

The objective of this investigation is to analyze singles prompt gamma de-excitation spectra, which are spectra recorded with one detector, resulting from thermal-neutron activation of an enriched sample of rhenium metal powder. The purpose is to obtain an improved understanding of the nuclear structure of the ^{186}Re isotope. The results may provide significant updates to the nuclear data libraries.

1.4 Hypothesis

The measurements of the $^{185}\text{Re}(n,\gamma)^{186}\text{Re}$ reaction performed in this work will provide confirmations and revisions to the nuclear data libraries, including the Evaluated Gamma Activation File (EGAF), the Reference Input Parameter Library (RIPL), and the Evaluated Nuclear Data File (ENDF).

1.5 Scope

This investigation was limited to the analysis of $^{185}\text{Re}(n,\gamma)^{186}\text{Re}$ spectra recorded at the Prompt Gamma Activation Analysis (PGAA) facility of the Budapest Research Reactor (BRR) and development of the resultant decay scheme. Also, initial statistical modeling was conducted using the Monte Carlo computer code DICEBOX, which generates simulated level-decay schemes [6]. The experimental measurements will ultimately be accompanied by and compared to the results of a complete set of

simulations. Agreement between the modeled level population and the measured level depopulation provides for the fidelity of the measurements.

1.6 Approach

The $^{185}\text{Re}(n,\gamma)^{186}\text{Re}$ spectra were fit using the spectral analysis software program Hypermet-PC. The broad range of gamma energies resulting from the (n,γ) reaction necessitated the use of fitted spectra from seven other nuclide standards, for which the decay schemes are well known, in order to generate a viable nonlinearity in channel correction and an efficiency calibration. Then, a spectrum was taken whose gain permitted measurement of gamma rays over a range of 0 to 11 MeV, since it was expected that some gamma rays could reach energies as high as 6.18 MeV. However, ^{186}Re is an odd-odd nucleus, which means that it has an odd number of protons and an odd number of neutrons, causing it to have a high density of low-lying energy levels. Therefore, a second spectrum was obtained with a higher gain, and correspondingly smaller energy range (0 to 865 keV), to focus more on distinguishing the lower-energy transitions. For each spectrum, a two-point energy and shape calibration was conducted based on the selection of two prominent and well-defined singlets, one in the low end of the spectrum and one in the high. A singlet is a peak that is not convolved with other neighboring peaks. Afterward, the aforementioned nonlinearity correction and efficiency calibration were applied. Following a methodical and precise peak fitting of the more than 1200 peaks in the rhenium spectra, a peak list was generated.

An exhaustive evaluation was made of all peaks in the spectrum such that the source of each peak was identified to the extent possible. The measured peak areas,

standardization to well-known comparator lines, correction for self absorption, and correction for abundance allowed for the deduction of partial gamma ray-production cross sections, which characterize the probability of the production of a given gamma ray for one nucleus of the examined chemical element [7]. Then, peaks due to the small amount of ^{187}Re present in the sample, beam background, escape, and summation were identified and separated from the peaks resulting from $^{185}\text{Re}(n,\gamma)^{186}\text{Re}$. It should be noted that sum peaks occur when a gamma cascade possesses an intermediate excited state that is extremely short-lived relative to the detector response time such that both gammas are recorded coincidentally [8].

The remaining peaks resulting from $^{185}\text{Re}(n,\gamma)^{186}\text{Re}$ were compared to the known transitions listed in the Evaluated Nuclear Structure Data File (ENSDF) and the Prompt Gamma-ray Spectrum Catalog [9]. There also remained peaks of unknown origin from which new primary transitions were proposed based on the binding-energy test. That is, the energy of an observed previously unidentified gamma-ray peak, when corrected for nuclear recoil, corresponded to the energy difference between the capture state and an ENSDF-adopted level. In addition, several energy levels were proposed for measured transitions that did not terminate at an adopted level. Next, a comprehensive level-decay scheme detailing the de-excitation of ^{186}Re was developed. It includes energy levels, level spin-parity, depopulation gamma-ray energies, partial gamma ray-production cross sections, internal conversion coefficients, transition multipolarities, and all relevant uncertainties. An arithmetic mean of the adopted and proposed primary transitions populating levels below 865 keV enabled a refinement of the neutron-separation energy. Furthermore, the decay scheme facilitated generation of an EGAF for ^{186}Re , which, in

turn, permitted simulation work with DICEBOX in order to generate preliminary validation of the experimental measurements. Finally, the measured partial gamma ray-production cross sections, along with the DICEBOX-computed contribution to ground-state population from the quasi-continuum, were used to derive a total radiative thermal neutron-capture cross section.

II. Theory

This chapter is organized into four parts. The first discusses the nuclear shell model as the basis for nuclear structure of deformed nuclei, such as ^{186}Re . The second part addresses compound nucleus formation as a result of thermal-neutron capture. It continues with an explanation of compound nucleus de-excitation via gamma-ray emission. The final portion consists of an overview of statistical gamma analysis, which is used to verify level-decay schemes and, by extension, understand nuclear structure.

2.1 Nuclear Models

The nuclear shell model, conceptually similar to the atomic shell model, was introduced in 1949 in order to describe the properties of nuclei [4]. While an oversimplified specification of nucleon behavior, it adheres to established physical/mathematical laws, accounts for previously determined nuclear properties, and predicts additional properties that are experimentally verifiable. The model characterizes nucleons according to their orbits and angular momentum. Moreover, the very fact that nuclear isomers exist validates the use of the shell model to describe the composition of the nucleus because nucleon orbits must carry a significantly high degree of angular momentum and isomers depend on the quantum numbers of those individual orbits [4]. That being said, the standard nuclear shell model, which treats the nucleus as a sphere, fails to fully explain deformed nuclei. In fact, because ^{186}Re is an odd-odd heavy nucleus (i.e., it has an odd number of both protons and neutrons and is over 150 amu), it is amongst the most complexly structured of nuclei. Specifically, the level density in the low-energy region is inordinately high due to the relatively low energies required to

excite unpaired nucleons. Nuclei that consist solely of paired nucleons require higher energies for excitation because of the need to overcome binding energy of paired nucleons [10].

As previously mentioned, the standard nuclear shell model assumes that the nuclear potential is spherical. This is not the case for nuclei with mass numbers A in the range of $150 \leq A \leq 190$ and $A > 230$. There are significant effects to shell structure in instances where there is strong deviation from physical symmetry [11]. The shell model potential associated with these nuclei is essentially an approximation of their rotational-ellipsoidal shape. A non-spherical potential applied within the Schrödinger equation invalidates the use of quantum number ℓ and, in turn, spectroscopic notation in the categorization of energy states as is done with spherical potentials [12]. Unlike the spherical case, in which the $2j + 1$ possible alignments of the \mathbf{j} vector, or the degeneracies, are equivalent in energy, the energy levels of a deformed potential depend on the spatial orientation of the orbit. This translates into a dependency on the projection of the angular momentum vector \mathbf{j} that is along the symmetrical axis of the core, denoted by Ω . These components possess reflection symmetry, which means Ω takes on both positive and negative values that are equal in magnitude and the degeneracy of the levels is 2 [12]. An example is shown in Figure 1, where $j = 7/2$. For the prolate case, the orbit with the smallest Ω , which is the most rotation-aligned value of \mathbf{j} , interacts most robustly with the core, meaning it is the most tightly bound and possesses the lowest energy. With respect to the oblate case, the orbit with the maximum Ω , which is the most deformation-aligned value of \mathbf{j} , interacts most strongly and is of the lowest energy [10, 12].

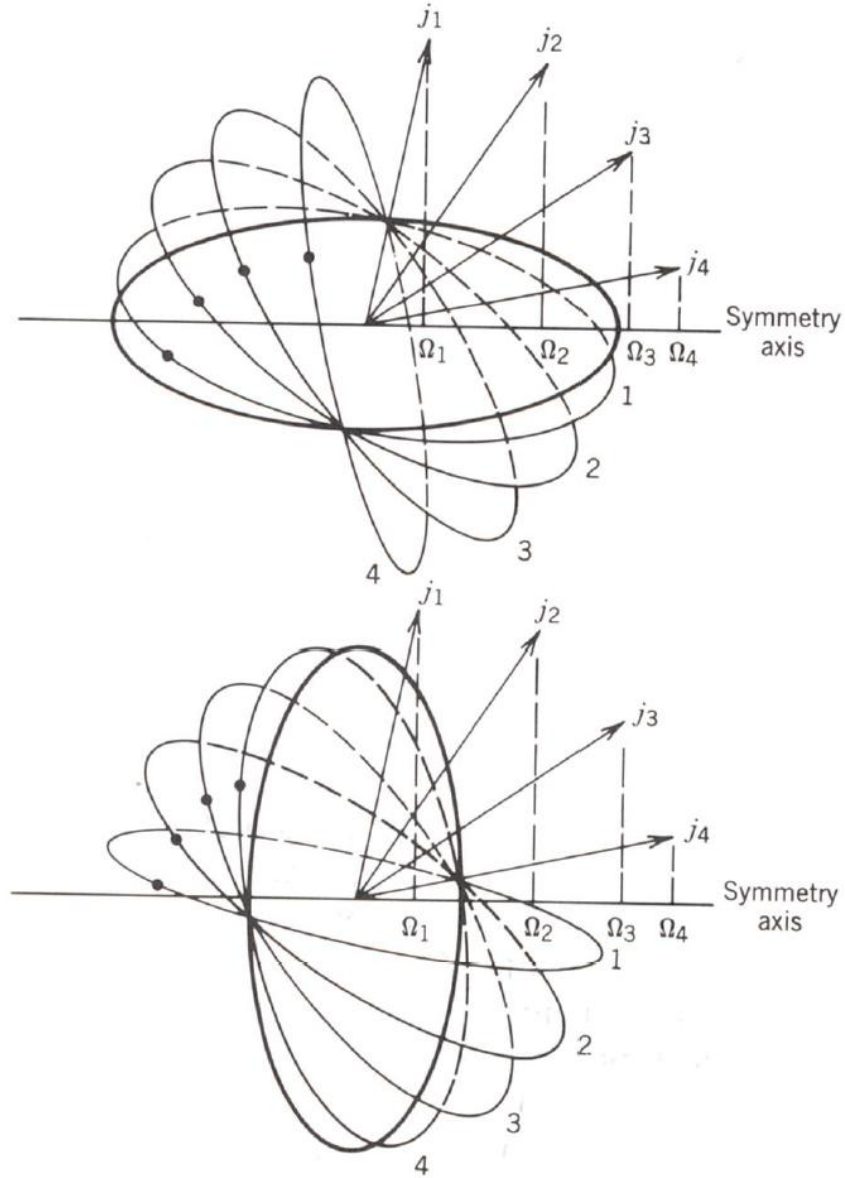


Figure 1. Single-particle orbits with $j = 7/2$ for both prolate (top) and oblate (bottom) deformations. In this case, there are four possible projections for Ω : $\pm 1/2$, $\pm 3/2$, $\pm 5/2$, and $\pm 7/2$. Reproduced with permission from [12].

^{186}Re is a prolate nucleus with high Ω single-particle orbitals near the Fermi surfaces, which are the boundaries between quantum states, for both protons and neutrons [13].

The general concept is graphically displayed by Figure 2.

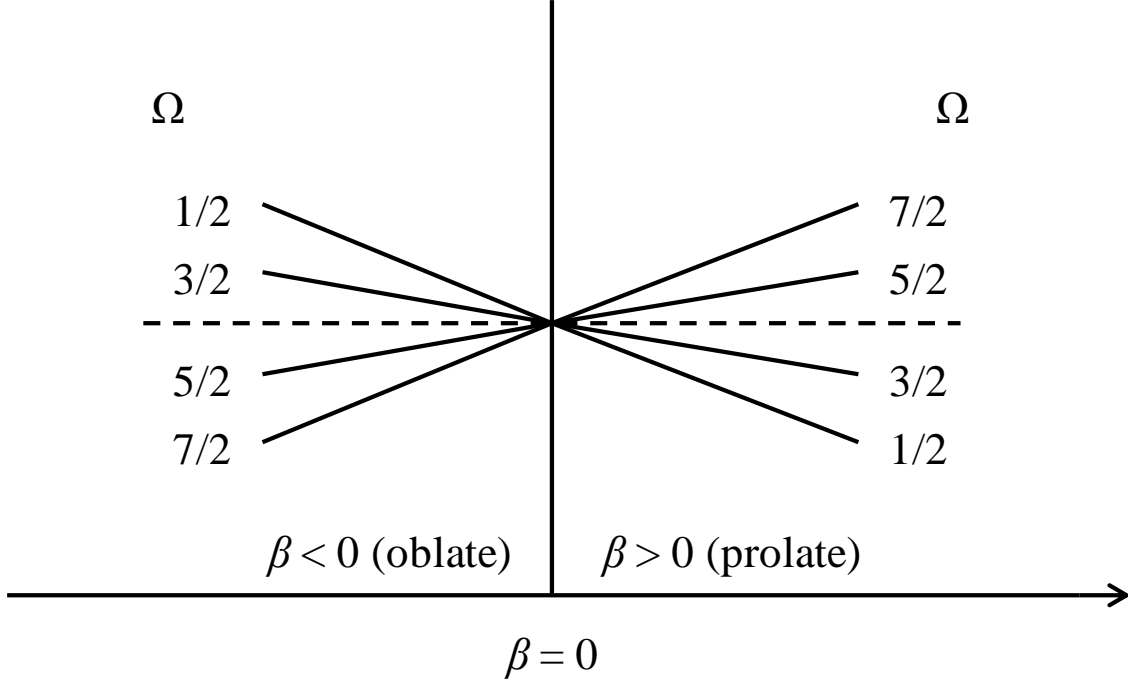


Figure 2. Possible values of Ω at various orientations. For a prolate core, $\Omega = 1/2$ marks the strongest interaction. By contrast, $\Omega = 7/2$ interacts more strongly with the oblate core. Adapted from [12].

The unique combination of high Ω single-particle orbital positions and the fact that ^{186}Re possesses a high density of levels at low excitation energies provides for an abundance of nuclear structure. Moreover, the former condition also contributes to the presence of low-lying excited states that have half-lives that are substantially longer than that of the ground state [13]. The significantly long half-life and the low excitation energy of the ^{186}Re metastable state relative to its ground state is evidence of this phenomenon.

Figure 1 and Figure 2 are not entirely applicable to the scenario at hand because the quantum numbers ℓ and j are spherical and, consequently, not valid under a deformed potential. In the example portrayed by the figures, where $j = 7/2$, $\Omega = 5/2$ is not identifiable in the f_4 state because the wave function of that state is a linear combination of multiple unique values of ℓ and j . Thus, the states from different oscillator shells do

not mix [12]. Returning to the example, the $\Omega = 5/2$ state only consists of input from the 5th oscillator shell as the $2f_{7/2}$ state is reached and the deformation parameter β approaches zero. With opposite parities, the 4th and 6th oscillator shells will not blend and the subsequent odd parity shells are sufficiently far away such that they do not significantly mix [12]. The deformed wave equation takes the form

$$\Psi'(\Omega) = \sum_{\ell j} a(N\ell j) \Psi_{N\ell j}, \quad (1)$$

where $\Psi'(\Omega)$ is the deformed wave function for state Ω , $a(N\ell j)$ is the expansion coefficient, and $\Psi_{N\ell j}$ is the spherical wave function. Expansion coefficients are ascertained by solving the Schrödinger equation for the deformed potential. These values vary with β and, in the case of the example, as $\beta \rightarrow 0$ it is expected that $a(5, 3, 7/2)$ will approach one while all other a approach zero [12]. With respect to the ^{186}Re nucleus, the deformation parameter is approximately 0.22, indicating moderately strong deformation. Furthermore, the mass region in which it is located is characterized by a relatively rapid change in deformation as a function of mass number [14].

A deformed nucleus may rotate in a sequence of states built on each single-particle state following the $I(I + 1)$ energy spacing, where I is angular momentum. The rotational band of the lowest state occurs at $I = \Omega$ and increases in rotational energy leads to added angular momentum of the form $I = \Omega, I = \Omega + 1, I = \Omega + 2 \dots$ [12]. An example of this is depicted in Figure 3, where three rotational bands, each having a unique proton-neutron configuration, are exhibited.

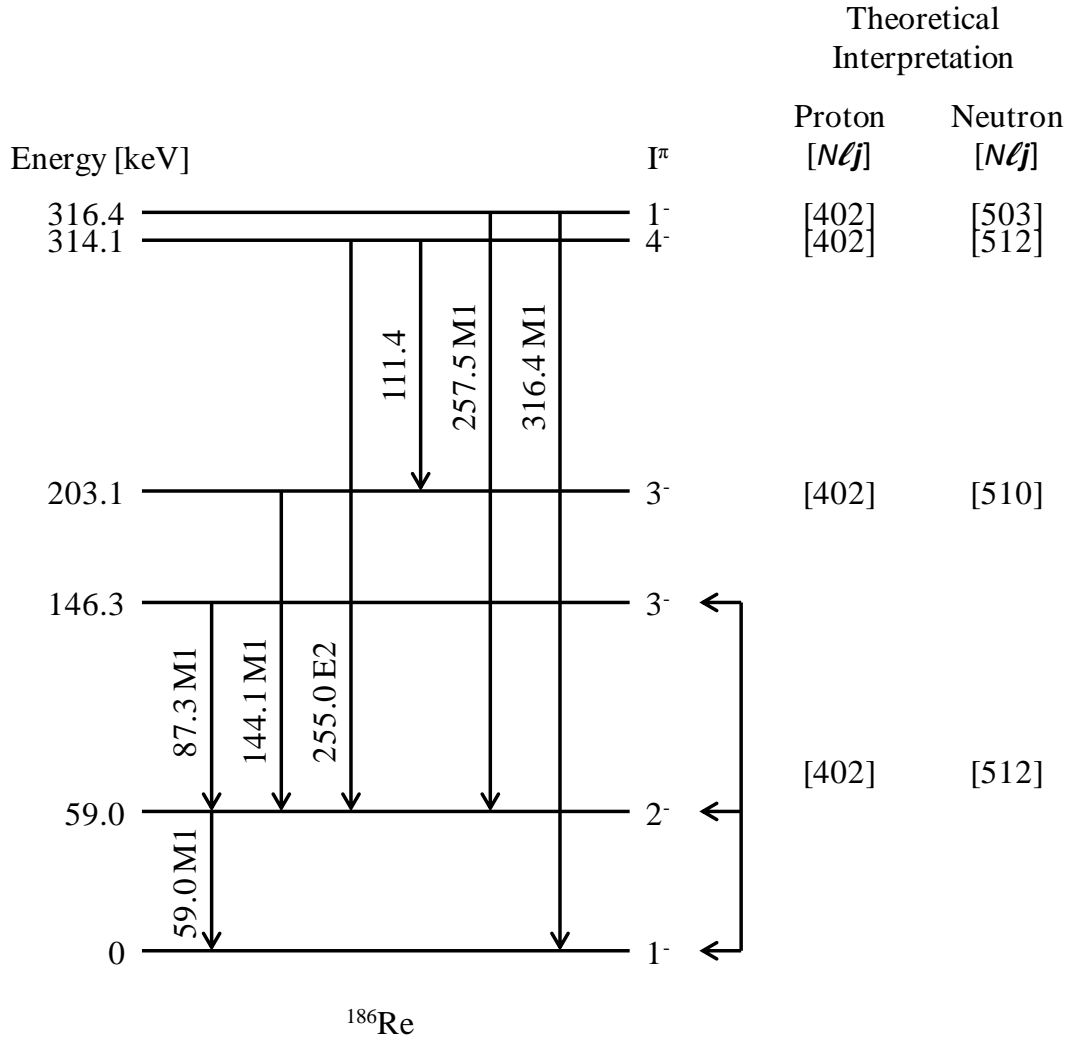


Figure 3. Theoretical energy level configuration of ^{186}Re via the coupling of the 75th proton to the 111th neutron. It accounts for some, but not all aspects of the observed scheme. Adapted from [14].

Figure 4 portrays single-particle states and their energies that are relevant to the Nilsson configuration of the ^{186}Re metastable-excited state. These types of configurations are named after S. G. Nilsson, the first person to solve the Schrödinger equation for the deformed potential, and they vary with the degree of deformation of nuclei in the $150 \leq A \leq 190$ mass range [12].

2.2 Compound Nucleus Formation via Thermal-neutron Capture

The (n, γ) reaction studied in this work describes thermal-neutron capture, which results in the formation of a compound nucleus as shown by



where n is the incident neutron, X is the chemical symbol of the target nucleus, Z is its atomic number, A is its mass number, and $*$ indicates that the reaction-product nucleus possesses excitation energy. The formula for the ${}^{185}\text{Re}(n,\gamma){}^{186}\text{Re}$ reaction is



The process is characterized by Bohr's theory of the compound nucleus, which is based on the extreme statistical model. More specifically, it states that the neutron interacts with the nucleus and strongly excites it. It then loses its identity as it shares its energy with the other nucleons. In terms of a quantum explanation, the nucleus is a system of nucleons arrayed in different orbits per given values of energy and angular momentum. The incoming neutron interacts with the other nucleons according to the selection rules resulting from the Pauli exclusion principle and conservation of energy, angular momentum, and parity [15].

Like all nuclear reactions, the (n, γ) reaction adheres to nucleon conservation. That is, the number of protons and neutrons must balance on either side of the equation. However, they do undergo a change in mass, which leads to a change in energy [16]. In the thermal ${}^{185}\text{Re}(n,\gamma){}^{186}\text{Re}$ reaction, the kinetic energies of the incident neutrons and

reaction-product nucleus are negligible. Therefore, conservation of energy dictates that the sensible change in energy is in the form of nuclear excitation energy E_{ex} as shown by

$$m_n c^2 + m_{185} c^2 = m_{186} c^2 + E_{ex}, \quad (4)$$

where m is mass, and c is the speed of light. Evaluation of Equation (4) in terms of atomic mass units (u) gives

$$E_{ex} = (1.00866501 + 184.952951 - 185.954984) c^2 \quad (5)$$

and solving for E_{ex} yields 6.18 MeV, where the mass-energy equivalence is $1u = 931.4943 \text{ MeV}/c^2$. When the kinetic energies are negligible, E_{ex} is due to the excess binding energy provided to the nucleus by the captured neutron and it is distributed amongst many nucleons such that no one nucleon escapes.

Beyond its energetics, the reaction occurs probabilistically. That is to say, there is a distinct probability that an incident neutron will interact with the target nucleus, which is defined in terms of the cross section for a given interaction. All reaction cross sections, including neutron capture, exhibit a high degree of dependence on neutron energy. For thermal ($< 0.025 \text{ eV}$) neutrons, the dependence typically embodies the $1/v$ law, which states that the cross section is inversely proportional to the neutron velocity as illustrated in Figure 5.

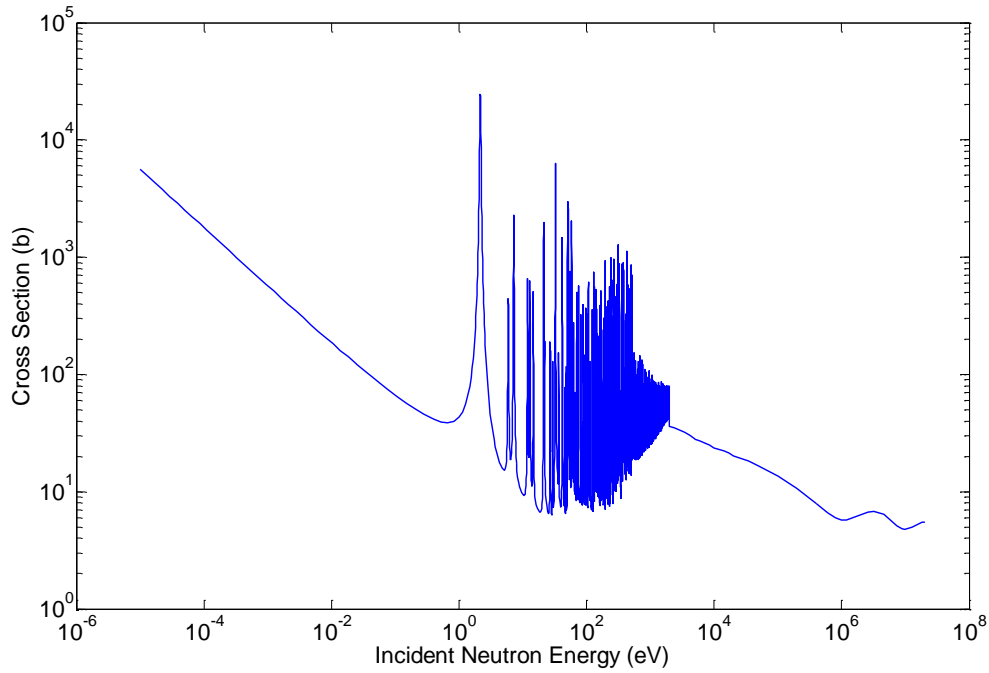


Figure 5. Total cross section of ^{185}Re . The $1/v$ law dependence is evident from 0 eV until approximately 0.025 eV. Adapted from [17].

Generally, the capture cross sections are compiled for a neutron velocity of 2200 m/s for thermal neutrons with energies of 0.025 eV. The $1/v$ law holds until just prior to the first resonance peak, marking the beginning of the epithermal region, which typically characterizes neutrons in the 1-eV to 1-keV range and the likelihood for reaction is high interspersed with periods of damping [7]. In the case of thermal capture, there is a high probability that one of the discrete quantum energy levels within the compound nucleus will be populated [12].

2.3 Gamma-ray Decay and Internal Conversion

2.3.1 Gamma-ray Decay

Following thermal-neutron capture, the compound nucleus is produced at high excitation energy and its most likely decay mechanism is via statistical gamma-ray

emission. The gamma rays are emitted over a range of energies up to the neutron-separation energy [12]. The process of gamma decay adheres to the laws of energy and momentum conservation as given by

$$\begin{aligned} E_i &= E_f + E_\gamma + T_R \\ 0 &= \vec{p}_R + \vec{p}_\gamma, \end{aligned} \tag{6}$$

where E_i is the initial excited state, E_f is the final state, T_R is the nucleus recoil energy, \vec{p}_R is the corresponding recoil momentum, and \vec{p}_γ is the momentum of the gamma ray [12]. The energy difference between the states $E_i - E_f$, which is also known as the transition energy ΔE , is found via

$$\Delta E = E_\gamma + \frac{E_\gamma^2}{2Amc^2}, \tag{7}$$

where E_γ is the gamma-ray energy [MeV] and A is the mass number of the reaction nucleus. The second term on the right hand side of Equation (7) represents nuclear recoil energy T_R . With respect to ^{186}Re , in cases where E_γ is below 1 MeV, nuclear recoil is generally negligible and $E_\gamma \approx \Delta E$. Due to the large atomic mass associated with ^{186}Re , the Mössbauer effect, where a gamma ray is emitted or absorbed by a nucleus free of recoil, is also negligible [10].

Besides determining gamma energies associated with de-excitation from the capture state, another key consideration is the partial gamma ray-production cross section σ_γ , which is determined by

$$\sigma_{\gamma} = \theta \sigma_0 P_{\gamma}, \quad (8)$$

where θ is the natural abundance of the isotope in the element of interest, σ_0 is the elemental-capture cross section, and P_{γ} is the gamma-ray emission probability. Essentially, P_{γ} represents the probability of one nucleus emitting a gamma ray and it follows the same energy dependence as the capture cross section [7].

Before continuing further on this subject, it is worth noting that there are three types of transitions: primary, secondary, and ground-state transitions, which is also a subset of the first two. Primary transitions are those beginning at the capture state, secondary transitions are those from intermediate levels, and ground-state transitions are those whose destination level is the ground state. Two or more back-to-back transitions are referred to as a cascade. Parent level population and branching ratios establish gamma-ray intensity, which is embodied by the previously mentioned quantity P_{γ} . This probability is not directly measured, but rather it is the ratio of the partial gamma-ray cross section to the capture cross section [7].

The sum of transition probabilities for all primary transitions should equal the total decay probability from the capture state and the sum of transition probabilities for ground-state transitions should equal the total decay probabilities from the capture state (unless there is a metastable-excited state) as demonstrated in

$$\begin{aligned}\sum_i P_{\gamma, j_i} &= 1 \\ \theta \sum_i \sigma_{\gamma, j_i} &= \sigma,\end{aligned}\tag{9}$$

where the index j_i is the subset of either primary or ground-state transitions [10]. Due to the difficulty in distinguishing between primary and ground-state transitions in prompt gamma spectra, the binding-energy test is often conducted. That is, the sum of all gamma-ray energies, each multiplied by their respective emission probabilities, must equal the neutron-separation energy S_n as shown by

$$\begin{aligned}S_n &= \sum_i E_{\gamma, i} P_{\gamma, i} \\ \sigma &= \theta \sum_i \frac{E_{\gamma, i}}{S_n} \sigma_{\gamma, i}.\end{aligned}\tag{10}$$

Here, the recoil energies are neglected, as the error associated with its approximation is significantly less than that attributed to unobserved gamma rays [7].

While a quantum characterization is more suitable for describing nuclear radiation, it is important to consider the classical explanation beforehand. Charge distributions are subject to multipole moments, be they dipole, quadrupole, etc., which generate oscillating electric and magnetic fields. Electric and magnetic multipoles are commonly denoted by E and M , respectively. A static electric dipole is comprised of two charges that are equal, opposite, and at a fixed distance from one another. A magnetic dipole is a circular current loop enclosing an area. Charge distributions that vary with time produce radiation fields [12]. These two types of dipoles and the fields they create are illustrated in Figure 6, which demonstrates that the cross product of vectors \mathbf{E} and \mathbf{B} ,

respectively representing the electric and magnetic fields, gives the direction of the radiation field.

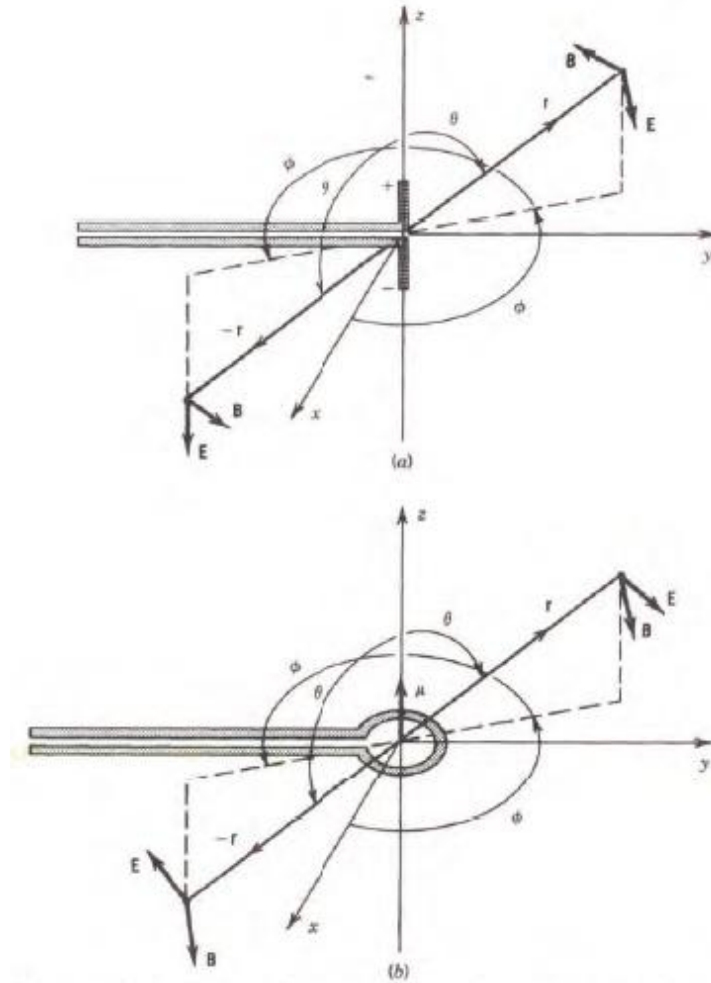


Figure 6. Electric and magnetic fields generated by an electric dipole (top) and a magnetic dipole (bottom), respectively. Vector E represents the electric field and vector B is the magnetic field. Reproduced with permission from [12].

There are three principles that govern multipole radiation fields. First, by introducing a radiation index L , the multipole order is defined as 2^L ($L = 1$ for dipole, $L = 2$ for quadrupole, etc) and its angular distribution relative to a chosen direction is dictated

by Legendre polynomials. Secondly, the parity π of electric and magnetic multipoles of the same L is always opposite as shown by

$$\begin{aligned}\pi(ML) &= (-1)^{L+1} \\ \pi(EL) &= (-1)^L.\end{aligned}\tag{11}$$

Lastly, the radiated power of electric or magnetic radiation is commensurate with

$$P(XL) = \frac{2(L+1)c}{\varepsilon_0 L [(2L+1)!!]^2} \left(\frac{\omega}{c} \right)^{2L+2} [m(XL)]^2,\tag{12}$$

where X is either E or M , $m(XL)$ is the amplitude of the moment, and ω is the circular frequency [12].

The same conditions apply quantum mechanically. However, the sources or multipole moments of the fields are quantized. This is done by replacing the multipole moments with multipole operators. The amplitude of the moment $m(XL)$ in Equation (12) takes the form

$$m_{fi}(XL) = \int \Psi_f^* m(XL) \Psi_i d\nu,\tag{13}$$

where $m_{fi}(XL)$ is the operator associated with the difference between the initial and final states, Ψ_f is the wave function of the final state, Ψ_i is the wave function of initial state, and ν is volume. The purpose of the operator corresponds to the change in the nuclear state and the creation of a photon with an energy, parity, and multipole order [12]. Since Equation (12) is the electromagnetic energy radiated per unit time, dividing out by energy

$\hbar\omega$ yields Equation (14), which is the emission probability per unit time, or the decay constant:

$$\lambda(XL) = \frac{P(XL)}{\hbar\omega} = \frac{2(L+1)}{\varepsilon_0 \hbar L [(2L+1)!!]^2} \left(\frac{\omega}{c} \right)^{2L+1} [m_{fi}(XL)]^2. \quad (14)$$

Incorporating a simplified single-particle radial component into the electric multipole transition gives

$$\lambda(EL) \cong \frac{8\pi(L+1)}{L[(2L+1)!!]^2} \frac{e^2}{4\pi\varepsilon_0 \hbar c} \left(\frac{E}{\hbar c} \right)^{2L+1} \left(\frac{3}{L+3} \right)^2 c \left(R_0 \sqrt[3]{A} \right)^{2L}, \quad (15)$$

where E is the energy in MeV, R_0 is the Bohr radius, and A is the mass number [12].

This expression is simplified by setting $R = R_0 A^{1/3}$ in order to provide an approximate solution. For the lower order electric multipoles, the decay constant, or Weisskopf, estimates are

$$\begin{aligned} \lambda(E1) &= 1.0 \times 10^{14} A^{2/3} E^3 \\ \lambda(E2) &= 7.3 \times 10^7 A^{4/3} E^5 \\ \lambda(E3) &= 34 A^2 E^7 \\ \lambda(E4) &= 1.1 \times 10^{-5} A^{8/3} E^9. \end{aligned} \quad (16)$$

Turning to magnetic multipole transitions, the formula for the decay constant is similar to Equation (15), but takes the form

$$\lambda(ML) \cong \frac{8\pi(L+1)}{L[(2L+1)!!]^2} \left(\mu_p - \frac{1}{L+1} \right)^2 \left(\frac{\hbar}{m_p c} \right)^2 \frac{e^2}{4\pi\epsilon_0 \hbar c} \times \left(\frac{E}{\hbar c} \right)^{2L+1} \left(\frac{3}{L+2} \right)^2 c \left(R_0 \sqrt[3]{A} \right)^{2L-2}, \quad (17)$$

where μ_p is the proton-nuclear magnetic moment. Setting $\left(\mu_p - \frac{1}{L+1} \right)^2 = 10$ provides the magnetic Weisskopf estimates, which are

$$\begin{aligned} \lambda(M1) &= 5.6 \times 10^{13} E^3 \\ \lambda(M2) &= 3.5 \times 10^7 A^{2/3} E^5 \\ \lambda(M3) &= 16 A^{4/3} E^7 \\ \lambda(M4) &= 4.5 \times 10^{-6} A^2 E^9. \end{aligned} \quad (18)$$

The Weisskopf estimates show that lower-order multipoles prevail over higher ones. As multipole order increases, the transition probability falls by a factor of approximately 10^{-5} per unit of increase. Moreover, they also demonstrate that electric radiation is more common than magnetic radiation by approximately two orders of magnitude for any given multipole order [12]. However, the Weisskopf estimates are often in error when compared to experimentally-measured values. An example of this are $E2$ transitions due to collective nuclear rotation that exhibit decay rates 10^2 greater than that predicted by the Weisskopf estimates, which are based on single-particle wave functions [10].

At this point, it is appropriate to examine the effects of momentum conservation on gamma emission. Each photon transfers an angular momentum $L\hbar$ for any particular

multipole L . An initial excited state of a nucleus with angular momentum I_i and parity π_i transitions to a final state with I_f and parity π_f while adhering to conservation per $I_i = L + I_f$. These vectors must form a closed triangle, which limits the values that L can take, the largest of which is $I_i + I_f$ and the smallest is $|I_i - I_f|$. The type of radiation, be it electrical or magnetic, depends on the relative parity of the initial and final states. No change in parity indicates that the radiation field has even parity, whereas a change in parity equates to a radiation field with odd parity. Electric multipoles have different parities than magnetic multipoles. By extension, if L is even, then electric fields have even parity and magnetic fields have odd parity. Conversely, if L is odd, then electric fields have odd parity and magnetic fields have even parity. To summarize, this translates into even electric multipoles and odd magnetic multipoles if parity does not change during the transition and odd electric multipoles and even magnetic multipoles if parity does change. The conditions imposed by angular momentum and parity in transitions are known as selection rules [12]. The selection rules determine whether certain transitions are allowed or forbidden and they are expressed as

$$\begin{aligned}
 |I_i - I_f| &\leq L \leq I_i + I_f \quad (\text{no } L = 0) \\
 \Delta\pi &= \text{no: even electric, odd magnetic} \\
 \Delta\pi &= \text{yes: odd electric, even magnetic.}
 \end{aligned}
 \tag{19}$$

It should be noted that, quantum mechanically, the initial and final states include spherical harmonics, so a transition from one state to another mediated by the electromagnetic field contains an integral of a triple product of spherical harmonics. The

products vanish unless certain conditions on $L1$, $L2$, and $L3$ are met, which lead to the selection rules [10].

Classifying multipoles, which enables the determination of energy-level spin, requires specific experimental techniques. Measuring just the energy of emitted photons (i.e. using only one detector) provides no information with respect to the angular distribution of radiation and, hence, no information about multipole orders [12]. Two techniques used to assess multipole order are low-temperature nuclear orientation and angular correlation. Low-temperature nuclear orientation consists of cooling nuclei to approximately 0.01 K and placing them in a strong magnetic field in order to create non-uniformity in the distribution of radiation, thereby permitting discrimination of the multipole orders. The second method entails measuring the angular distribution of emitted gammas relative to one another so as to create an unequal mixture of populations, which also provides information about multipole order composition [12]. In order to categorize the radiation type, be it electric or magnetic, additional special techniques are required, such as linear polarization distribution measurements. This involves establishing the directional relationship between the axis of the emitting nucleus, direction of emitted radiation, and its electric field [12]. Only through the use of these methods, in addition to measuring gamma-ray energy and intensity, can the full structure of the nucleus be understood.

2.3.2 Internal Conversion

Internal conversion is a process that competes with gamma emission. It occurs when the electromagnetic multipole fields of the nucleus do not cause photonic emission, but instead interact with the atomic electrons causing electron emission. In this case, the

transition energy ΔE is equivalent to the kinetic energy of the emitted electron T_e minus its binding energy B_e . The total decay probability Γ_t is then equal to the probability of gamma emission Γ_γ plus the probability of conversion Γ_e [12]. Additionally, internal conversion is the prevalent process for low-energy transitions. As a general rule, the lower the transitional energy and the higher the mass, the more heavily converted the transition is. However, it is considered negligible for transition energies exceeding 400 keV. Internal conversion is accounted for via the internal conversion coefficient α and it is defined as $\alpha = \Gamma_e / \Gamma_\gamma$ [12]. Calculating this coefficient is a formidable task and it is dependent on the atomic number, transition energy, uncertainty in energy, multipolarity, multipole mixing ratio (only for mixed transitions), and uncertainty in mixing ratio. The probability of total decay is then determined by $\Gamma_t = \Gamma_\gamma (1 + \alpha)$.

2.4 Statistical Gamma Analysis

In some cases, experimental measurements alone are insufficient in establishing the structure of nuclei. This is particularly true for odd-odd heavy nuclei, such as ^{186}Re . As excitation energy increases, the number of levels per unit of energy also increases. In other words, the spacing between the levels diminishes and their nature becomes very complicated. Therefore, the use of a statistical model is an effective manner by which to describe them (see, i.e. Reference [18]). A model that serves to characterize nuclear structure is a generalization of the extreme statistical model proposed by Bohr in his concept of the compound nucleus [19]. In this vein, the implementation of a Monte Carlo method may be useful to simulate gamma-ray cascades following compound nucleus formation [20].

The modeling method involves establishing a critical energy E_{crit} below which the level scheme is taken from experiment as it is assumed to be complete. This includes energies, spins, parities, and depopulation (de-excitation) transitions. Between E_{crit} and the capture state, which is known as the quasi-continuum, the level scheme is randomly generated based on an assumed level density (LD) model $\rho(E, J^\pi)$, where E is excitation energy and J^π is the level spin-parity assignment. The transitions from the quasi-continuum adhere to a chosen *a priori* photon strength function (PSF), which is denoted by $f^{(XL)}$, where XL is the transition multipolarity [20]. Selection rules are accounted for in the determination of allowed transitions from the quasi-continuum for all potential combinations of pairs of initial E_i and final E_f states per $E_\gamma = E_i - E_f$. As applicable, correction for internal conversion is required. The partial radiation widths Γ_{if}^{XL} , which are the decay rates associated with various transitions multiplied by Planck's constant of the non-forbidden transition probabilities, are assumed to follow a Porter-Thomas distribution [21] and its center lies on a mean value given by

$$\langle \Gamma_{if}^{(XL)} \rangle = \frac{f^{(XL)}(E_\gamma) E_\gamma^{2L+1}}{\rho(E_i, J_i^{\pi_i})}. \quad (20)$$

The random generation of a set of all Γ_{if}^{XL} is known as a nuclear realization, which describes the level-decay properties [6]. Generally, statistically modeling the decay scheme entails performing 50 separate nuclear realizations (i.e. decay-scheme simulations), each consisting of 100,000 simulated capture state gamma ray-cascade events [20].

The intensity of simulated population transitions into the measured levels below E_{crit} should be approximately equivalent to the experimentally measured level depopulation transitions from those levels. Except in the case of an isomer, it should be noted that is not physical for level population to be greater than level depopulation. The population of these low-lying levels relies on four components: level density, the photon strength functions governing the various transition multipolarities, the experimental level scheme below E_{crit} , and the capture-state spin composition (see, i.e. Reference [6]). The experimentally measured σ_γ are used to normalize the simulated population per neutron capture in order to generate absolute cross sections. The total radiative thermal neutron-capture cross section σ_0 is the summation of all measured transitions feeding the ground state combined with the summation of all simulated transitions from the quasi-continuum feeding the ground state as exhibited by

$$\sigma_0 = \sum \sigma_\gamma^{\text{exp}}(GS) + \sum \sigma_\gamma^{\text{sim}}(GS) = \frac{\sum \sigma_\gamma^{\text{exp}}(GS)}{1 - P(GS)}, \quad (21)$$

where $\sum \sigma_\gamma^{\text{exp}}(GS)$ is the sum of experimental cross sections feeding the ground state, $\sum \sigma_\gamma^{\text{sim}}(GS)$ is the simulated contribution from the quasi-continuum, and $P(GS)$ is the simulated ground state population per neutron capture [20].

2.4.1 Level Density Models

Two level density models, the constant temperature formula (CTF) and the back-shifted Fermi gas (BSFG) formula are considered when randomly generating levels

above E_{crit} . Both models reflect a statistical method that adheres to the relationship between level density and excitation energy given by

$$N(E) = \int \rho(E) dE, \quad (22)$$

where $N(E)$ is the cumulative number density of levels and $\rho(E)$ is the density of levels at a given excitation energy E .

The CTF model assumes a constant temperature throughout the entire range of excitation energies and its explicit formula is

$$\rho(E, J) = \frac{f(J)}{T} \exp\left(\frac{E - E_0}{T}\right), \quad (23)$$

where T is the critical temperature necessary for breaking a nucleon pair. The parameter E_0 is the energy backshift related to the pairing of protons and neutrons. It is obtained by fitting the functional form of Equation (23) to the experimental level densities below E_{crit} and the average spacing of neutron (proton) resonances. The function $f(J)$ is the spin distribution factor, which may be expressed as

$$f(J) = \frac{2J+1}{2\sigma_c^2} \exp\left(-\frac{(J+1/2)^2}{2\sigma_c^2}\right), \quad (24)$$

where σ_c is the spin-cutoff parameter, which is proportional to the square root of the excitation energy and it is calculated via $\sigma_c = 0.98A^{0.29}$ [22, 23, 24].

The BSFG model, which assumes the nucleus acts as a fluid of fermions, or particles with half-integer spins, is written as

$$\rho(E, J) = f(J) \frac{\exp(2\sqrt{a(E - E_1)})}{12\sqrt{2}\sigma_c a^{1/4} (E - E_1)^{5/4}}, \quad (25)$$

where the parameters E_1 and a are the level-density parameter and the shell model level-density parameter, respectively. They may also be derived by fitting the functional form of Equation (25) to experimental data [23]. The spin-cutoff parameter used in combination with this model takes the form

$$\sigma_c^2 = 0.0146A^{5/3} \frac{1 + \sqrt{1 + 4a(E - E_1)}}{2a}. \quad (26)$$

At high excitation energies, such as within the quasi-continuum region, the level density is typically considered parity independent. However, at lower excitation energies, most nuclei exhibit some degree of parity dependence [25]. For the purposes of this work, the level parity is treated as entirely independent above E_{crit} .

2.4.2 Photon Strength Functions

Nuclear reactions cause nucleons to move in a complicated manner that couples with the electromagnetic field due to their electric- and magnetic-multipole moments. The dynamics of the nuclear system are caused by these strong interactions, yet they are not entirely understood and, therefore, nor is the process of gamma emission. While prediction of individual transition intensities is not possible, if the nucleus is large enough such that it radiates at many frequencies, gamma emission is described by photon strength functions (PSF), which predict average properties of the gamma-ray spectrum [18]. As mentioned in the discussion of gamma-decay mechanisms, gamma emission

occurs over an angular distribution described by the corresponding multipole moments. The most common multipole moments associated with gamma emission are $E1$, $M1$, and $E2$, each of which has an associated PSF.

Giant Dipole Electric Resonance

The electric dipole is the dominant multipole moment from neutron-capturing states above 5 MeV and they are described by a broad resonance structure in the strength function. This is particularly relevant to the ^{186}Re nucleus as the excitation energy of its capture state is 6.18 MeV. These $E1$ primary gamma-ray transitions are dominated by the low-energy tail of the giant dipole electric resonance (GDER), which results from a particular type of collective nuclear vibrations [18, 20]. The two models of the PSF describing the GDER considered in this work are the Brink-Axel (BA) and the Enhanced Generalized Lorentzian (EGLO) model.

The Brink-Axel model is predicated on the Brink hypothesis that the photoabsorption cross section is energy smoothed and does not depend on the initial excitation energy of the nucleus [26]. The BA model is a form of the standard Lorentzian distribution given by

$$f_{BA}^{(E1)}(E_\gamma) = \frac{1}{3(\pi\hbar c)^2} \sum_{i=1}^{i=2} \frac{\sigma_{Gi} E_\gamma \Gamma_{Gi}^2}{(E_\gamma^2 - E_{Gi}^2)^2 + E_\gamma^2 \Gamma_{Gi}^2}, \quad (27)$$

where E_{Gi} [MeV] is the centroid of the resonance, Γ_{Gi} [MeV] is the width of the resonance, σ_{Gi} [mb] is the resonance cross section, and the coefficient prior to the summation is equal to $8.68 \times 10^{-8} \text{ mb} \cdot \text{MeV}^{-2}$. The summation is executed for two sets

of resonance parameters $i = 1$ and $i = 2$, which represent the vibrations along the axis of symmetry and those perpendicular to the axis of symmetry, respectively [20].

The EGLO model, on the other hand, violates the Brink hypothesis since it invokes a dependence on nuclear temperature Θ , which is a function of excitation energy per $\Theta = \sqrt{(E_{ex} - \Delta)/a}$, where E_{ex} is the excitation energy of a final state, Δ is the pairing energy, and a is the shell model level-density parameter (described earlier). For odd-odd nuclei, $\Delta = -0.5 \cdot |P_d|$, where $|P_d|$ is the deuteron pairing energy and may be found in Reference [23]. The EGLO model takes the form

$$f_{EGLO}^{(E1)}(E_\gamma, \Theta) = \sum_{i=1}^{i=2} \frac{\sigma_{Gi} \Gamma_{Gi}^2}{3(\pi \hbar c)^2} \left[F_K \frac{4\pi^2 \Theta^2 \Gamma_{Gi}^2}{E_{Gi}^5} + \frac{\sigma_{Gi} E_\gamma \Gamma_{Gi}(E_\gamma, \Theta)}{(E_\gamma^2 - E_{Gi}^2)^2 + E_\gamma^2 \Gamma_{Gi}^2(E_\gamma, \Theta)} \right], \quad (28)$$

where $\Gamma_{Gi}(E_\gamma, \Theta)$ is the functional form of nuclear temperature. In this model, GDERs that are based on excited states may vary quite significantly from those based on the ground state because the width of the resonance is also a function of nuclear temperature,

$$\Gamma_{Gi}(E_\gamma, \Theta) = \underbrace{\left(k_0 + (1 - k_0) + \frac{E_\gamma - E_0}{E_{Gi} - E_0} \right)}_{EGLO} \underbrace{\left(\frac{\Gamma_{Gi}}{E_{Gi}^2} (E_\gamma^2 + 4\pi^2 \Theta^2) \right)}_{GLO}, \quad (29)$$

where the parenthesized term on the right is the standard General Lorentzian Model (GLO) as proposed by Reference [27], k_0 is the enhancement factor and E_0 is the reference energy. The only difference between f_{GLO} and f_{EGLO} is the left-parenthesized

term containing k_0 , the value of which is varied so as to provide optimal agreement with the absorption data [20].

Giant Dipole Magnetic Resonance

The giant dipole magnetic resonance (GDMR) is characterized by one of three principle models: single-particle, scissors, and spin-flip. The single-particle approach assumes the PSF is constant and independent of transition energy. The scissors model treats the $M1$ mode as a scissors-like counter rotation of the proton fluid versus the neutron fluid. It is also proposed that flip between orbits of a given shell, which is when the spin axis undergoes a sudden change, contributes to the $M1$. The various resonance modes are depicted in Figure 7.

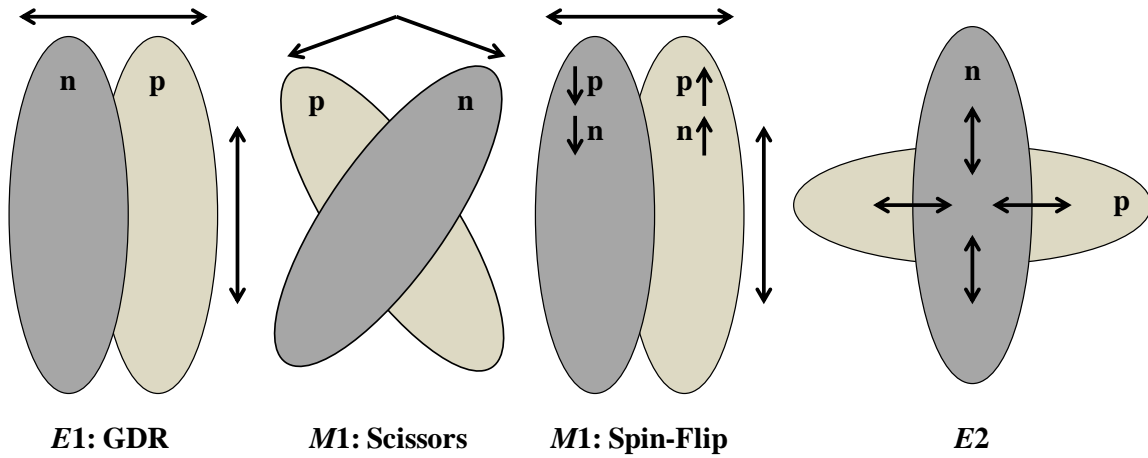


Figure 7. Illustration of giant resonance modes characterizing nuclear electromagnetic decay. The scissors mode is the magnetic equivalent of the GDER. Adapted from [18].

There is little experimental data available concerning the GDMR in ^{186}Re . However, contributions of $M1$ strength is expected to be significantly lower than the corresponding $E1$ contribution. Therefore, the single-particle approach is quite reasonable in this case (see, i.e. Reference [20]).

Giant Quadrupole Electric Resonance

A giant quadrupole electric resonance (GQER) model, which is also displayed in Figure 7, explains the PSF for $E2$ transitions. It is worth noting that quadrupole strength is significantly less than dipole strength. Nevertheless, it uses a Lorentzian distribution to portray an isoscalar-isovector quadrupole vibration. Like the GDER, it relies on the input of resonance parameters. Higher-order transitions, to include $M2$ and above, are generally not considered due to their infrequency [20].

III. Experimental Setup and Data Analysis Methodology

This chapter is divided into two sections. The first segment provides information about the experimental setup employed by the data collection team at the Prompt Gamma Activation Analysis (PGAA) facility, which is collocated with the Budapest Research Reactor (BRR). The second part offers an overview of the analytical method implemented for data evaluation.

3.1 Experimental Setup

The $^{185}\text{Re}(n,\gamma)^{186}\text{Re}$ experimental data were generated at the PGAA facility. The PGAA equipment included a target station, a Compton suppressed high-purity germanium (HPGe) gamma-ray spectrometer, a beam stop, and shielding to protect the detector and personnel [28]. Figure 8 is a schematic of the PGAA facility, which is collocated with the Neutron Induced Prompt Gamma-Ray Spectrometer (NIPS) facility.

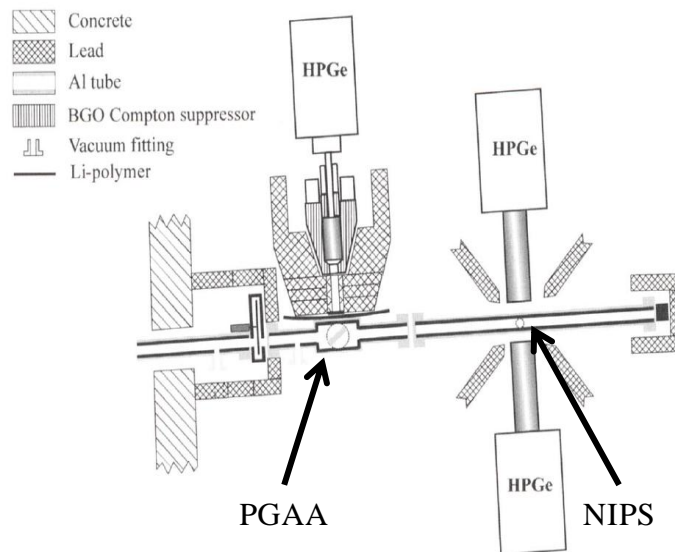


Figure 8. The PGAA and NIPS facilities. The PGAA facility is shown by the leftmost HPGe detector and the NIPS facility is the pair of detectors on the right. Reproduced with permission from [28].

The remainder of this section provides brief descriptions of the equipment items and the physical layout of the PGAA facility.

The BRR, shown in Figure 9, is a light-water moderated and cooled reactor that operates at 10 MW_t.



Figure 9. The 10 MW_t Budapest Research Reactor.

Typically, cold neutrons are used in PGAA because of the higher-capture cross sections associated with sub-thermal neutrons [28]. Cold neutrons are generated using a liquid-hydrogen cold source for moderation. At the sample position, the thermal equivalent-neutron flux is ordinarily $5 \times 10^7 \text{ n} \cdot \text{cm}^{-2} \cdot \text{s}^{-1}$ [29]. However, the cold source was not functioning during the $^{185}\text{Re}(n,\gamma)^{186}\text{Re}$ experiment and a thermal-neutron flux of $2.3 \times 10^6 \text{ n} \cdot \text{cm}^{-2} \cdot \text{s}^{-1}$ with an effective temperature of approximately 120 K was achieved at the target station.

The neutrons travel from the reactor to the target station via a nickel supermirror layered-neutron guide. The term supermirror indicates that the guide was lined with a high number of Bragg reflecting layers, which are critical for maintaining low incident-angle neutron transmission over long distances. The neutrons then traverse the shutter position, which is comprised of a boron carbide absorber. There are also two individual shutters, one each for the PGAA beam and the NIPS beam, which are constructed of highly-enriched ^6Li plastic [28]. Next, the neutrons enter a three meter evacuated-aluminum beam tube that collimates the beams to either 2×2 or $1 \times 1 \text{ cm}^2$. The beam used in the $^{185}\text{Re}(n,\gamma)^{186}\text{Re}$ experiment was collimated to $2 \times 2 \text{ cm}^2$. The $3 \times 5 \text{ m}^2$ sample chamber is located 1.5 meters from the guide tube. Generally, it is maintained with a vacuum, ^4He , or other gaseous atmospheres to lower background radiation caused by neutrons. For the $^{185}\text{Re}(n,\gamma)^{186}\text{Re}$ measurements, air served as the environment. The target station, which is located within the chamber and approximately 35 meters from the reactor wall, consists of an aluminum frame with Teflon suspension strings from which the sample is mounted [29]. At the rear of the chamber, neutrons are absorbed by a highly-enriched ^6Li backstop [28].

The spectrometer employed for the experiment was an *n*-type HPGe detector with closed end-coaxial geometry and it was positioned approximately 23 cm from the sample [20]. Figure 10 portrays the target station and spectrometer positions.



Figure 10. The PGAA target station and Compton-suppressed HPGe detector.

Additionally, a bismuth germanate (BGO) annulus and 10 cm of lead shielding surrounded the detector in order to suppress the effects of Compton scattering. Figure 11 is a diagram of the detector system.

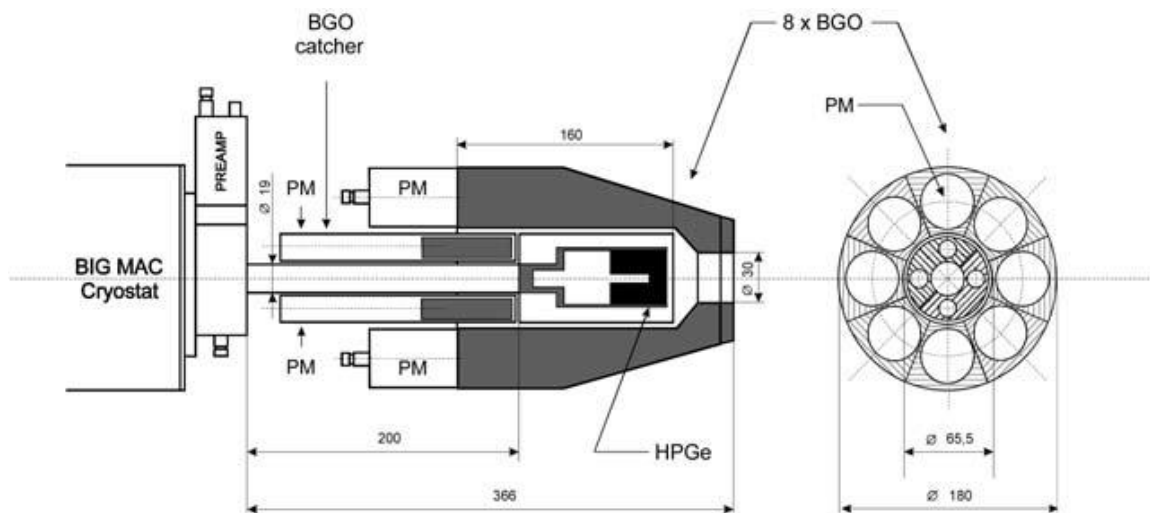


Figure 11. Diagram of the PGAA facility *n*-type HPGe detector with BGO Compton suppressor. Reproduced with permission from [29].

The BGO device and catchers detect the scattered photons and, when operated in anti-coincidence with the detector, a Compton-suppressed spectrum is obtained [29]. Bismuth germanate is the preferred scintillating material for this purpose as its high density and atomic number allow for a relatively compact configuration and high interaction probability. Additionally, the thin contacts of an *n*-type detector minimize the absorbing material that can potentially attenuate scattered photons between the inner detector (HPGe) and outer detectors (BGO) [30].

Enriched ^{185}Re metal powder (96.74% ^{185}Re and 3.26% ^{187}Re) produced by Oak Ridge National Laboratory served as the target material, the assay for which is contained in Appendix A. It was arranged so as to maximize homogeneity, its mass was 0.15076 g, its dimensions were 10 mm \times 10 mm, and it was approximately 0.1 mm thick. Further discussion of the *effective* sample thickness exposed to the neutron beam follows in the subsequent section. Figure 12 depicts preparation of the sample.



Figure 12. Preparation of the enriched ^{185}Re metal powder target. The target was contained in a small Teflon bag and adjusted such that homogeneity was maximized without having to incorporate a solvent.

Recording of the first of the two spectra analyzed in this work commenced at 1803 hrs local time on November 9th, 2010 and concluded at 0936 hrs the following morning with a live time of 55,996 s. The second spectrum, recorded with an increase in gain, was collected from 1139 to 1511 hrs on November 12th with a live time of 12,936 s.

3.2 Data Analysis Methodology

The method implemented for analyzing the data consists of several processing steps that recur until a specific condition is met. The step-by-step procedure is illustrated in Figure 13.

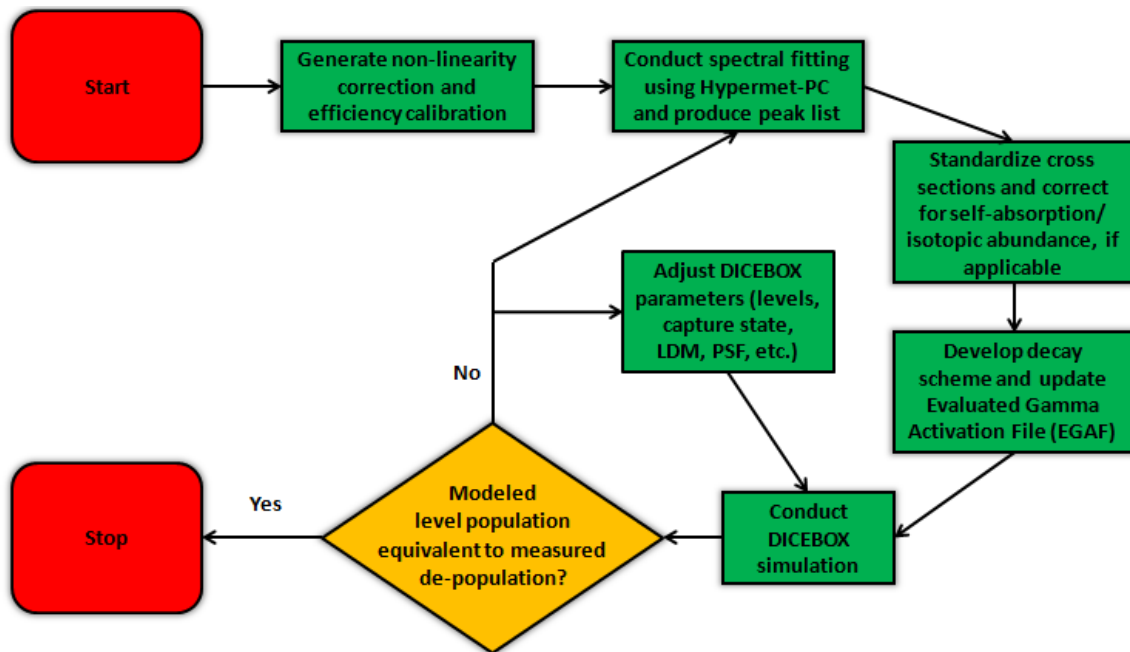


Figure 13. Flow chart of the data analysis procedure. The green rectangles are processing steps and the amber diamond is the conditional or decision point.

The remainder of this section will briefly elaborate on each of the steps.

The progression begins with the generation of a nonlinearity in channel correction and efficiency calibration using Hypermet-PC. A more thorough discussion of the

correction and calibration development follows in the next chapter. The spectral data file is then loaded; a two-point energy and shape calibration is conducted with one peak in the low-energy region of the spectrum and the other in the high-energy region. In practice, the two selected peaks should be well-defined singlets. Next, the nonlinearity correction and efficiency calibration files (discussed later) are loaded, followed by the execution of an automatic fit of the entire spectrum. All peak fits are manually inspected for goodness of fit, starting from the high-energy region and working backward through the low-energy region. An example of manual inspection is exhibited in Figure 14.

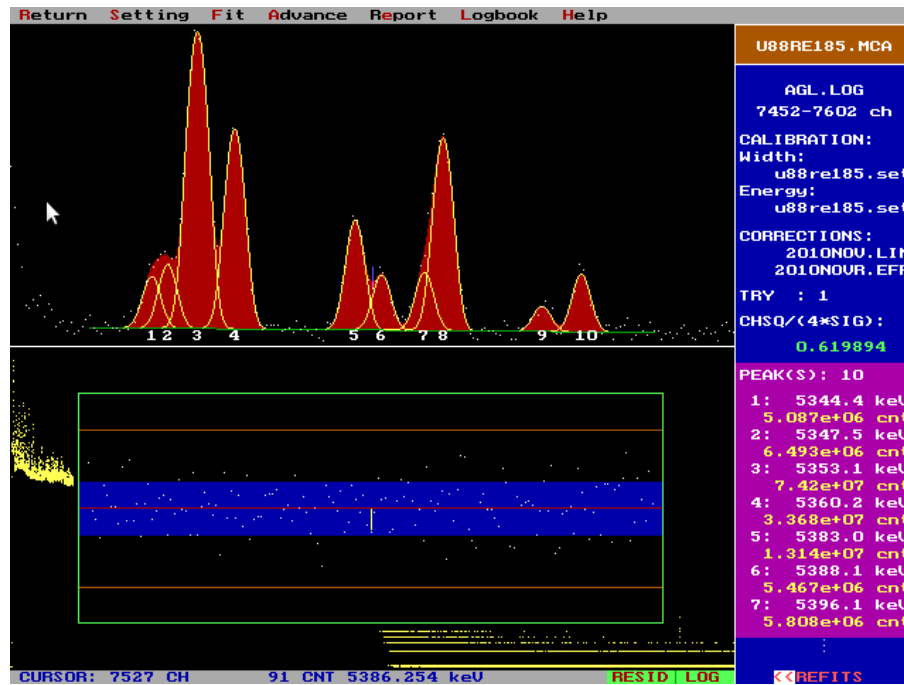


Figure 14. Inspection of peaks within a region for goodness of fit. The region displayed above encompasses peaks within the 5340 to 5400 keV energy range. The lower half of the screen contains the residuals corresponding to the various fits.

If a fit is not visually and/or statistically satisfactory, the region of interest limits are adjusted, additional peaks may be added or deleted, and/or the background characterization is altered. The final step of the fitting routine involves generating a peak

list that includes peak energies, uncertainties in energy, peak intensities, and uncertainties in intensity. It is worth noting that the uncertainty in energy is comprised of the statistical error associated with fitting peaks via a modified Gaussian distribution, along with the error contributed by the nonlinearity correction and the energy calibration. The uncertainty in intensity is due to statistical error and error from the efficiency calibration [10, 31, 32].

The partial gamma ray-production cross section σ_γ is determined via a standardization procedure, which entails normalizing the measured intensities by scaling them to well known comparator lines [33]. The cross sections contained in this work were derived from the comparator cross sections of three distinct ^{186}Re gamma lines, which were obtained from Reference [9], and they are listed in Table 1.

Table 1. Elemental comparator cross sections used in the standardization procedure.

E_γ [keV]	σ_γ [b]
144.152(5)	1.8(3)
214.647(4)	2.53(14)
316.457(9)	2.21(10)

Due to a complete dependence on $1/v$ for thermal neutrons, correcting the cross sections for neutron beam temperature was not required [20]. However, a small correction was required for self absorption. Self absorption occurs when gamma rays resulting from an (n,γ) reaction inside the sample are completely, or partially, attenuated within it. ^{185}Re is amongst the most physically dense of isotopes at 21.02 g/cm^3 . By contrast, the physical density of ^{207}Pb , the predominant isotopic constituent of natural lead, is 11.34 g/cm^3 [34]. Therefore, the vast majority of the (n,γ) reactions take place at or near the sample surface,

thereby mitigating the likelihood of self absorption. Nevertheless, after determining the non-uniform effective sample thickness by iteratively varying the sample thickness until the standardized cross section for the 87-keV gamma line converged with that from a previous measurement of ReCl_3 , a small correction for self absorption was determined and applied to the measurements contained in this work [31]. It should be noted that self absorption was negligible in the ReCl_3 measurement. Lastly, an isotopic abundance correction was performed.

The next step involved developing the complete decay scheme for the energy levels below 865 keV and the primary decay sequence from the capture state, which is displayed and discussed in the following chapter. The level information consists of the measured level energies $E_{L\text{-}exp.}$, literature (ENSDF)-level energies $E_{L\text{-}lit.}$, uncertainties in energy, the difference between measured level energies and their associated literature level energies ΔE , and the spin-parity assignments J^π per literature. The decay or depopulation gamma-ray information from each level includes gamma energies E_γ , uncertainties in energy, σ_γ , uncertainties in σ_γ , internal conversion coefficients α , uncertainties in α , and the transition multipolarities per literature.

The measured energy levels were determined through the application of a linear least-squares fit to the level data, which included correction for nuclear recoil. The Band-Raman Internal Conversion Coefficient calculator (BrIcc) was utilized to calculate α [35]. The input into BrIcc comprises atomic number, gamma-ray energy, uncertainty in energy, multipolarity, and, in the case of a mixed multipolarity, the mixing ratio with its uncertainty. Lastly, conducting level-intensity balance checks and comparing the measured relative intensities to those in the ENSDF was an effective means by which to

preliminarily validate the cross sections and, by extension, the decay scheme. Following decay-scheme development, the Evaluated Gamma Activation File (EGAF) was generated. The EGAF data, which is displayed in Appendix B, are augmented using the ENSDF [2]. The EGAF data are used to normalize the DICEBOX statistical-modeling results.

The primary objective of the DICEBOX calculations is to compare the simulated population against the measured depopulation in order to assess the quality of the decay-scheme data. All possible combinations of level density (LD) models and photon strength functions (PSF) that were described in the previous chapter were examined [20]. Additionally, various aspects of the capture state and the spins of individual levels below the critical energy E_{crit} were manipulated. Spectral refits were also required from time to time in order to refine several σ_γ . Generally, when varying these parameters and updating cross sections, one executes ten realizations with 20,000 events per realization. Once all cross sections are validated to the extent possible and the appropriate LD model and PSF have been adopted such that the simulated population and measured depopulation exhibit equivalency within the allotted uncertainty (3σ), the number of realizations is increased to 50 and the number of events per realization to 100,000 in order to increase statistical significance.

IV. Results and Discussion

This chapter is organized into seven parts. The first section provides information on the calibrations implemented during spectral analysis. It is followed by an overview of the observed high-energy decay scheme. The subsequent segment contains the results for the observed low-energy region. Then, the statistical-modeling parameters and outcomes are discussed. The chapter continues with a detailed analysis of the first fifteen excited states. The ensuing section discusses the neutron-separation energy calculation based on primary gamma-ray transition measurements. Finally, it concludes with a proposal for a new and independently measured thermal neutron-capture cross section.

4.1 Nonlinearity Correction and Efficiency Calibration

For the purposes of PGAA, the low-energy region (<1 MeV) and the high-energy region (generally above 5 MeV) are of the most interest. This is due to the density of transitions and the highly-energetic primary transitions that occur in each case, respectively. In the low-energy region, the density of peaks is such that accuracy in energy of ± 0.1 keV is required, whereas in the high-energy region accuracy to within 0.5 to 1 keV is sufficient. Therefore, in order to obtain accurate peak positions over the entire energy range (0 – 11 MeV), a correction for the spectrometer system nonlinearity is required. Without this correction, systematic errors (up to 1 keV) in peak position would occur [36]. Likewise, an efficiency correction curve is also necessary in order to obtain accurate gamma-ray intensities. These two corrections take the form of multi-parameter functions and are generated biannually at the BRR using standard radioactive and reaction sources: ^{133}Ba , ^{152}Eu , ^{207}Bi , ^{226}Ra , ^{241}Am , $^{14}\text{N}(n,\gamma)^{15}\text{N}$, and $^{35}\text{Cl}(n,\gamma)^{36}\text{Cl}$

spectra. These spectra enable correction over both the low- and high-energy regions. Application of these corrections then allows for a simple two-point energy and shape calibration, utilizing a well-defined singlet in each region.

4.1.1 Nonlinearity Correction

The Hypermet-PC nonlinearity correction developed for this experiment is displayed in Figure 15.

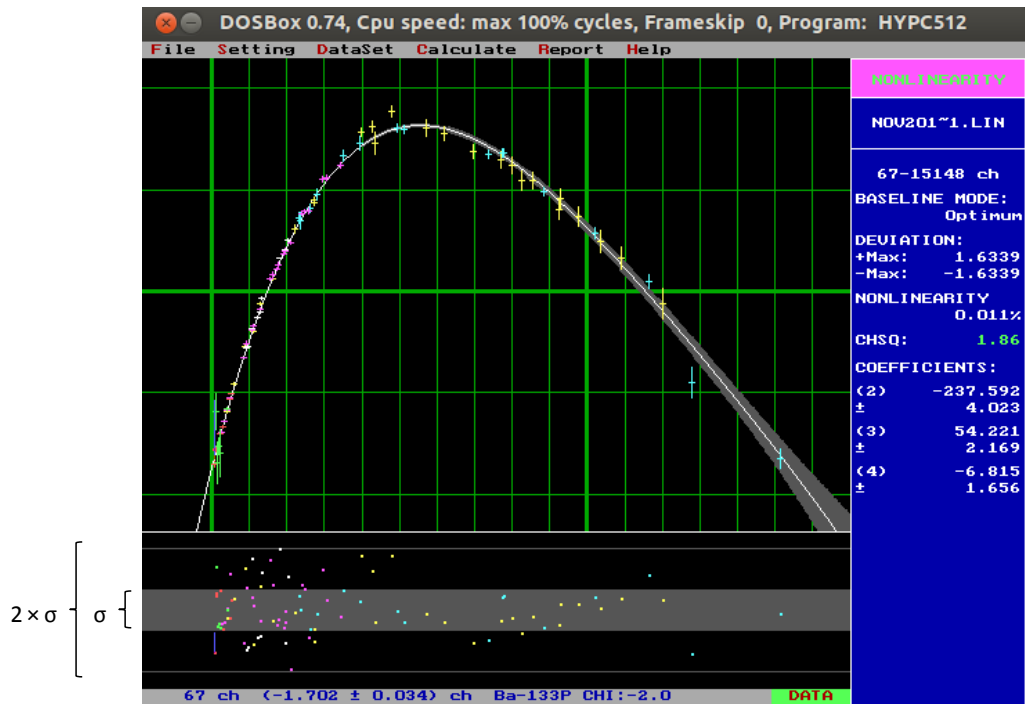


Figure 15. Hypermet-PC nonlinearity in channel correction. The residuals of the fit are shown below the curve. The curve coefficients and goodness of fit are listed along the right hand side. The residuals are all within two standard deviations of the fit.

Data points representative of the high-energy region were obtained via $^{14}\text{N}(n,\gamma)^{15}\text{N}$ and $^{35}\text{Cl}(n,\gamma)^{36}\text{Cl}$ prompt gamma-ray reactions. The decay gamma rays from ^{133}Ba , ^{152}Eu , ^{207}Bi , ^{226}Ra , and ^{241}Am radioactive sources formed the data points for the densely populated low-energy region. The fitting function is a fourth order polynomial and all

residuals are within two standard deviations. Furthermore, a goodness of fit χ^2 of 1.86 indicates that the correction is statistically acceptable. It is worth noting that the correction is applicable for both the ^{186}Re spectrum taken with an increase in gain and the ^{186}Re spectrum recorded without a gain increase. While all parts of the signal processing chain play a role in system nonlinearity, the contribution of the analog-to-digital converter (ADC) dominates and the effect due to increasing amplifier gain is negligible [32].

4.1.2 Efficiency Calibration

Figure 16 exhibits the Hypermet-PC absolute detector efficiency correction generated in order to accurately determine gamma-ray intensities.

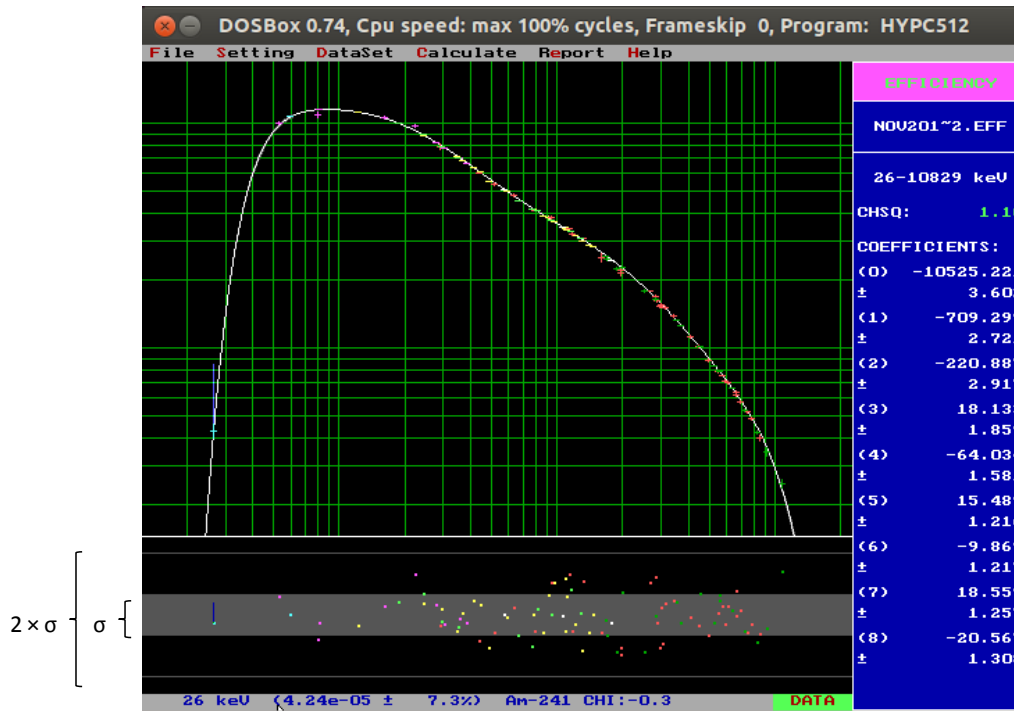


Figure 16. Hypermet-PC detector efficiency correction. The residuals of the fit are shown below the curve. The curve coefficients and goodness of fit are listed along the right hand side. The residuals are all within two standard deviations of the fit.

As with nonlinearity, the high-energy data points are from the (n, γ) spectra. The numerous data points from the decay gamma spectra, particularly those from the ^{133}Ba and ^{241}Am , facilitate accurate characterization of gamma-ray intensities in the low-energy region. While a relative efficiency calibration is sufficient, the efficiency was absolutely calibrated based on the known activity of the ^{152}Eu source, to which all other spectra were normalized. The function that fits the data points is an eighth order polynomial, no residual exceeded two standard deviations, and the χ^2 was 1.10.

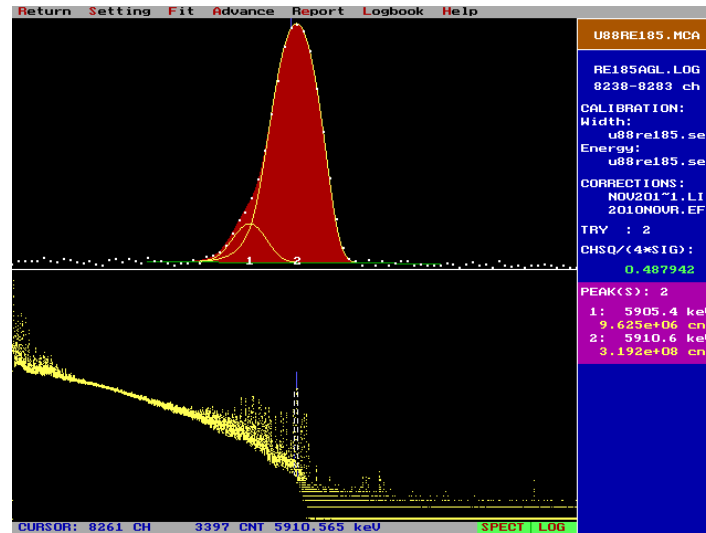
4.2 High-energy (n, γ) Spectrum

The binding-energy test was employed for the purpose of confirming previously identified primary transitions and for proposing new ones. The test entails subtracting the energy of an observed gamma ray and the corresponding nuclear recoil energy from the excitation energy of the capture state, which is equivalent to the amount of energy required to remove a neutron from the nucleus S_n , in order to obtain the remaining excitation energy $E_{Exc.}$ [12]. The explicit formula is

$$E_{Exc.} = S_n - E_\gamma + T_R, \quad (30)$$

where E_γ is the gamma-ray energy and T_R is the kinetic energy of nucleus recoil. If the calculated $E_{Exc.}$ corresponds to an ENSDF-adopted energy level, then it is highly probable that the observed gamma ray is the result of a primary transition. A practical example from this work is shown in Figure 17.

1. A peak is observed at 5905.4 ± 0.2 keV. When factoring in nuclear recoil, the corresponding transition energy is 5905.5 ± 0.2 keV



2. There is not a corresponding gamma-ray listed in the ENSDF for the $^{185}\text{Re}(n,\gamma)^{186}\text{Re}$ reaction.
3. However, there is an adopted energy level at 273.627 ± 0.005 keV.

E_γ^a	E_{level}	$I_\gamma^{\# \&}$	$E_{\text{level}}^{\#}$	J^π	$T_{1/2}^@$
5801.5	6179.8	0.034 18	268.798 ^a 6	(4)-	
5858.3	6179.8	0.25 6	273.627 ^d 5	(4)-	
5911.3	6179.8	1.14 24	314.009 ^e 5	(3)+	24.1 ns 11

4. The adopted excitation energy of the neutron capture state is 6179.7 ± 0.7 keV.

Adopted Levels, Gammas

Published: 2003 Nuclear Data Sheets.

$$Q_\beta = 1069.5 \text{ 9 } S_n = 6179.7 \text{ 7 } S_p = 5830.3 \text{ 11 } Q_\alpha = 2078.0 \text{ 21 } \text{1995Au04}$$

5. Calculation:

$$(6179.7 \pm 0.7 \text{ keV}) - (5905.5 \text{ keV} \pm 0.2 \text{ keV}) = (274.2 \pm 0.7 \text{ keV})$$

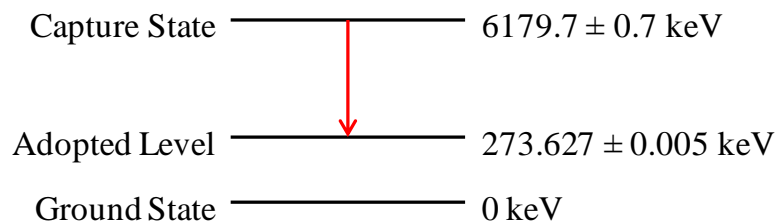


Figure 17. An example of the binding-energy test. The difference between the adopted capture state and the measured transition corresponds to an adopted energy level, which indicates that there is a high likelihood that the observed transition is a primary transition.

The region of interest was confined to the energy range between 3917 keV and the capture state excitation energy, which is approximately 6180 keV. The lower limit was established because there are no adopted energy levels above 2622(4) keV, which is the destination level for the observed 3917.96(38)-keV gamma ray. Without an adopted level, the results of the binding-energy test are less conclusive.

Once peaks from $^{187}\text{Re}(n,\gamma)^{188}\text{Re}$, escape peaks, and background lines were identified and separated, the binding-energy test was performed on those remaining. Table 2 contains a list of all observed $^{185}\text{Re}(n,\gamma)^{186}\text{Re}$ gamma-ray energies above 3917 keV, along with the corresponding excitation energy of their respective destination levels and partial gamma ray-production cross sections σ_γ . As applicable, a comparison with ENSDF-adopted levels is presented. When an observed, yet unevaluated transition corresponded to an adopted level within one standard deviation, it was proposed as a new primary transition and enclosed in braces. In several instances, a transition was identified because, when added to another transition, the result was consistent with the neutron-separation energy. However, as previously mentioned, this case is less certain than when the energy of a transition from the capture state corresponds to the energy of an adopted level. Selection rules were also considered in the proposal of new primary transitions.

The ground state spin-parity assignment J_{GS} of ^{185}Re is $5/2^+$ and, following thermal-neutron capture, the compound nucleus spin-parity assignment is 2^+ or 3^+ per $J_{CS} = J_{GS} + \ell \pm s$, where $\ell = 0$ and $s = 1/2$. Therefore, because $E1$ transitions are most likely from capture states above 5 MeV, primary transitions are only allowed to states with a spin-parity J^π between 1^- and 4^- [14]. However, the J^π for all ^{186}Re states, except for the

ground state and the capture state, is tentatively assigned. Overall, this work resulted in the proposal of 54 new primary transitions, which is important information for the nuclear data libraries and, by extension, for applications such as nuclear forensics.

Table 2. Observed primary transitions in the ^{186}Re high-energy spectrum. The excitation energies were determined by subtracting the gamma-ray energies and the associated nuclear recoil energy from the adopted neutron-separation energy. The literature values for the energy levels and spin-parity assignments are from the ENSDF [2]. The cross sections are corrected for self absorption and abundance. Quantities in parentheses are uncertainties in significant figure format and quantities contained inside braces are proposals resulting from this work.

E_γ [keV]	$E_{\text{Exc.}}$ [keV]	$E_{L,\text{lit.}}$ [keV]	J^π	σ_γ [b]
6179.22(15)	0.37(17)	0	1^-	0.019(1)
6120.51(8)	59.08(11)	59.010(3)	2^-	0.123(8)
6080.14(8)	99.45(11)	99.361(3)	3^-	0.126(9)
6032.87(13)	146.72(15)	146.274(4)	3^-	0.062(6)
6005.45(12)	174.15(14)	173.929(4)	4^-	0.057(4)
5968.79(16)	210.81(17)	210.699(5)	2^-	0.016(1)
5910.60(8)	269.00(11)	268.798(6)	4^-	0.620(42)
{5905.44(20)}	274.16(21)	273.627(5)	4^-	0.019(4)
{5862.55(42)}	317.05(43)	316.463(12)	1^-	0.009(2)
5857.03(9)	322.57(11)	322.379(6)	3^-	0.144(10)
5800.81(12)	378.79(14)	378.392(12)	2^-	0.016(1)
5759.25(41)	420.35(42)	420.559(7)	4^+	0.002(1)
{5754.52(7)}	425.08(10)	425.823(7)	$2^+, 3^+, 4^+$	0.004(1)
5709.56(11)	470.05(13)	469.779(17)	4^-	0.120(9)
{5678.68(30)}	500.93(31)	500.722(16)	4^+	0.004(1)
5644.96(11)	534.65(13)	534.37(4)	4^-	0.080(6)
{5619.06(107)}	560.55(107)	559.976(9)	5^+	0.001(1)
5601.63(10)	577.98(12)	577.723(16)	2^-	0.114(8)
5493.41(8)	686.20(11)	686.058(17)	3^-	0.092(7)
{5425.95(24)}	753.67(25)	753.7	$2^-, 3^-$	0.011(1)
{5416.80(89)}	762.82(89)	761.42(19)	$1^-, 2^-, 3^-$	0.003(1)
{5395.80(37)}	783.82(38)	785.31(20)	2^+	0.008(1)
{5388.18(15)}	791.44(17)	791.5	1^-	0.012(1)
5383.16(10)	796.46(12)	796.63(20)	≤ 3	0.026(2)
5360.33(12)	819.29(14)	818.94(19)	$2^-, 3^-$	0.067(5)
5353.25(11)	826.37(13)	826.152(18)	4^-	0.146(10)
{5323.31(37)}	856.31(38)	855.04(5)	4^+	0.005(1)
5317.03(9)	862.59(11)	864.17(15)	$2^-, 3^-$	0.046(4)

E_γ [keV]	$E_{Exc.}$ [keV]	$E_{L-iii.}$ [keV]	J^π	σ_γ [b]
5306.88(10)	872.74(12)	871.3	-	0.424(3)
5284.44(9)	895.18(11)	895.0	2 ⁻ ,3 ⁻ ,4 ⁻	0.073(5)
5277.15(8)	902.47(11)	901.8	2 ⁻ ,3 ⁻	0.146(10)
5255.94(18)	923.6(19)	923.7	2 ⁻ ,3 ⁻	0.095(1)
5244.15(18)	935.47(19)	935.5	2 ⁻ ,3 ⁻	0.039(4)
{5231.92(60)}	947.70(60)	946.4	2 ⁻ ,3 ⁻	0.003(1)
5206.72(13)	972.90(15)	975.0	-	0.063(6)
{5190.49(13)}	989.13(15)	988.8	2 ⁻ ,3 ⁻	0.014(2)
{5180.08(30)}	999.54(31)	999.3	2 ⁻ ,3 ⁻ ,4 ⁻	0.012(2)
5176.47(8)	1003.15(11)	1004.8	2 ⁻ ,3 ⁻ ,4 ⁻	0.155(11)
5139.29(10)	1040.13(12)	1039.9	2 ⁻ ,3 ⁻ ,4 ⁻	0.235(17)
5111.01(26)	1068.61(27)	1069.8	2 ⁻ ,3 ⁻	0.048(5)
5082.39(8)	1097.24(11)	1097.1	4 ⁻	0.054(4)
{5076.72(9)}	1102.91(11)	1102.9	2 ⁻ ,3 ⁻	0.081(6)
{5056.91(17)}	1122.72(18)	1123.9	2 ⁻ ,3 ⁻	0.026(3)
5047.34(12)	1132.29(14)	1131(5)		0.032(3)
{5038.64(21)}	1140.99(22)	1141.9	2 ⁻ ,3 ⁻	0.009(1)
5028.28(8)	1151.35(11)	1151.3	4 ⁻	0.267(19)
{5021.61(12)}	1158.02(14)	1157.6	2 ⁻ ,3 ⁻ ,4 ⁻	0.031(3)
5007.45(7)	1172.18(10)	1173.6	-	0.278(19)
4994.66(10)	1184.97(12)	1185.0	2 ⁻ ,3 ⁻	0.038(3)
4981.75(7)	1197.88(10)	1197.9	2 ⁻ ,3 ⁻	0.101(7)
{4951.66(14)}	1227.97(16)	1225.8	1 ⁻ ,2 ⁻ ,3 ⁻	0.041(4)
{4936.84(13)}	1242.79(15)	1242.1	2 ⁻ ,3 ⁻	0.104(11)
{4930.44(17)}	1249.19(18)	1248.5	-	0.016(2)
4915.58(9)	1264.05(11)	1261.3	1 ⁻	0.054(4)
{4911.40(10)}	1268.23(12)	1271.8	2 ⁻ ,3 ⁻ ,4 ⁻	0.016(2)
4893.53(23)	1286.10(24)	1285.4	2 ⁻ ,3 ⁻	0.016(2)
4872.06(12)	1307.57(14)	1307.5	-	0.069(5)
4862.11(10)	1317.52(12)	1317.9	2 ⁻ ,3 ⁻ ,4 ⁻	0.227(16)
{4857.49(10)}	1322.14(12)	1322.0	2 ⁻ ,3 ⁻	0.085(7)
4828.42(13)	1351.21(15)	1351.7	4 ⁻	0.038(5)
{4824.14(30)}	1355.49(31)	1355.2	2 ⁻ ,3 ⁻	0.016(3)
{4819.29(38)}	1360.34(39)	1359.5	2 ⁻ ,3 ⁻ ,4 ⁻	0.010(3)
4808.72(28)	{1370.91(29)}	-		0.0225(4)
{4793.33(12)}	1386.30(14)	1385.3	2 ⁻ ,3 ⁻	0.031(3)
4774.02(7)	1405.61(10)	1405.8	2 ⁻ ,3 ⁻ ,4 ⁻	0.229(16)
{4760.54(28)}	1419.09(29)	1419.4	2 ⁻ ,3 ⁻	0.016(2)
4741.60(18)	1438.04(19)	1437(4)		0.030(3)
4729.46(28)	1450.18(29)	1450.1	1 ⁻ ,2 ⁻ ,3 ⁻	0.011(1)

E_γ [keV]	$E_{Exc.}$ [keV]	$E_{L-lit.}$ [keV]	J^π	σ_γ [b]
{4722.14(14)}	1457.50(16)	1458.1	2 ⁻ ,3 ⁻	0.023(3)
{4717.42(32)}	1462.22(33)	1462.8	2 ⁻ ,3 ⁻	0.007(2)
{4704.25(21)}	1475.39(22)	1476.0	-	0.023(2)
4702.01(6)	{1477.63(9)}	-		0.011(3)
4692.90(9)	1486.74(11)	1489(5)		0.047(5)
4662.39(2)	{1517.25(21)}	-		0.030(4)
{4654.57(12)}	1525.08(12)	1525.7	4 ⁻	0.051(5)
{4647.04(22)}	1532.60(23)	1531.4	2 ⁻ ,3 ⁻	0.010(1)
{4639.98(69)}	1539.66(69)	1538.8	1 ⁻ ,2 ⁻ ,3 ⁻	0.004(1)
4634.85(7)	1544.79(10)	1545.0	-	0.096(7)
{4629.21(12)}	1550.43(14)	1550.9	1 ⁻ ,2 ⁻ ,3 ⁻	0.029(2)
4613.16(20)	1566.48(21)	1566.6	2 ⁻ ,3 ⁻ ,4 ⁻	0.049(7)
{4607.45(13)}	1572.19(15)	1572.1	1 ⁻ ,2 ⁻ ,3 ⁻	0.034(6)
{4602.58(27)}	1577.06(28)	1575.8	2 ⁻ ,3 ⁻ ,4 ⁻	0.018(6)
4592.42(8)	{1587.22(11)}	-		0.054(4)
{4586.63(13)}	1593.01(15)	1591.6	2 ⁻ ,3 ⁻	0.020(2)
4573.16(28)	1606.48(29)	1608(4)		0.026(5)
4551.65(12)	1627.99(14)	1627.3	2 ⁻ ,3 ⁻ ,4 ⁻	0.022(2)
{4534.61(18)}	1645.03(19)	1643.9	1 ⁻ ,2 ⁻ ,3 ⁻	0.031(3)
4531.93(17)	1647.71(18)	1648.1	2 ⁻ ,3 ⁻ ,4 ⁻	0.028(3)
{4519.89(37)}	1659.75(38)	1662.1	-	0.019(4)
4513.79(28)	1665.85(29)	1667.8	2 ⁻ ,3 ⁻ ,4 ⁻	0.021(2)
{4507.41(10)}	1672.23(12)	1672.8	1 ⁻ ,2 ⁻ ,3 ⁻	0.062(5)
4502.18(11)	{1677.46(13)}	-		0.030(2)
{4496.15(10)}	1683.49(12)	1684.2	2 ⁻ ,3 ⁻ ,4 ⁻	0.034(3)
{4479.14(13)}	1700.50(15)	1696.5	2 ⁻ ,3 ⁻	0.025(2)
{4467.47(43)}	1712.17(44)	1711.1	2 ⁻ ,3 ⁻	0.007(1)
{4460.12(9)}	1719.52(11)	1719.1	2 ⁻ ,3 ⁻ ,4 ⁻	0.068(5)
4456.89(10)	{1722.75(12)}	-		0.061(4)
{4436.70(13)}	{1742.94(15)}	-		0.030(3)
{4422.41(23)}	1757.23(24)	1758.0	2 ⁻ ,3 ⁻	0.030(3)
4412.46(10)	1767.18(12)	1768(5)		0.044(4)
4388.05(20)	{1791.59(21)}	-		0.013(1)
{4384.06(12)}	1795.58(14)	1794.0	-	0.020(2)
{4363.57(60)}	1816.08(60)	1818.1	2 ⁻ ,3 ⁻ ,4 ⁻	0.011(2)
{4352.91(17)}	1826.74(18)	1828.1	2 ⁻ ,3 ⁻ ,4 ⁻	0.036(5)
{4339.82(40)}	1839.83(41)	1839.9	1 ⁻ ,2 ⁻ ,3 ⁻	0.016(4)
{4334.20(52)}	1845.45(52)	1847.3	2 ⁻ ,3 ⁻	0.020(6)
4298.36(13)	{1881.29(15)}	-		0.048(5)
{4290.74(21)}	1888.91(22)	1885(4)		0.014(2)

E_γ [keV]	$E_{Exc.}$ [keV]	$E_{L-lit.}$ [keV]	J^π	σ_γ [b]
4273.57(39)	1906.08(40)	1906(4)		0.015(2)
{4266.28(15)}	{1913.37(17)}	-		0.039(4)
4215.69(53)	1963.96(53)	1966(4)		0.031(12)
4197.40(26)	1982.25(27)	1985(4)		0.013(2)
{4188.17(26)}	{1991.48(27)}	-		0.012(2)
4179.49(13)	2000.16(15)	2005(4)		0.080(10)
4119.5(8)	2060.10(11)	2064(4)		0.058(4)
4097.23(19)	2082.42(20)	2083(4)		0.024(2)
4075.67(10)	2103.98(12)	2107(4)		0.049(4)
4038.37(5)	2141.28(9)	2142		0.006(2)
3976.36(23)	2203.29(24)	2205(4)		0.019(3)
3960.62(17)	2219.03(18)	2219(4)		0.024(5)
3934.97(12)	2244.69(14)	2246		0.043(4)
{3927.26(24)}	{2252.40(25)}	-		0.012(2)
3917.96(38)	2261.70(39)	2262(4)		0.010(2)

In summary, 69 previously known primary transitions were confirmed, 54 new primaries were identified, and 12 new energy levels were proposed. Generally, the cross sections of the newly-identified transitions were significantly lower than those of the adopted transitions, as expected. The fact that the weak proposed transitions were observed at all was likely due to the combination of the highly enriched sample, the low background, and the Compton-suppressed spectrometer.

4.3 Low-energy (n, γ) Spectrum

For the purposes of this work, an excitation energy of 865 keV was set such that all energy levels below it are characterized as constituents of the low-energy region of the (n, γ) spectrum. The rationale for establishing this upper limit is that the ENSDF-adopted level at 864.17 keV is amongst the last levels for which there is an adopted depopulation

gamma ray [2]. Figure 18 offers a visual representation of the population and depopulation of selected levels below 865 keV.

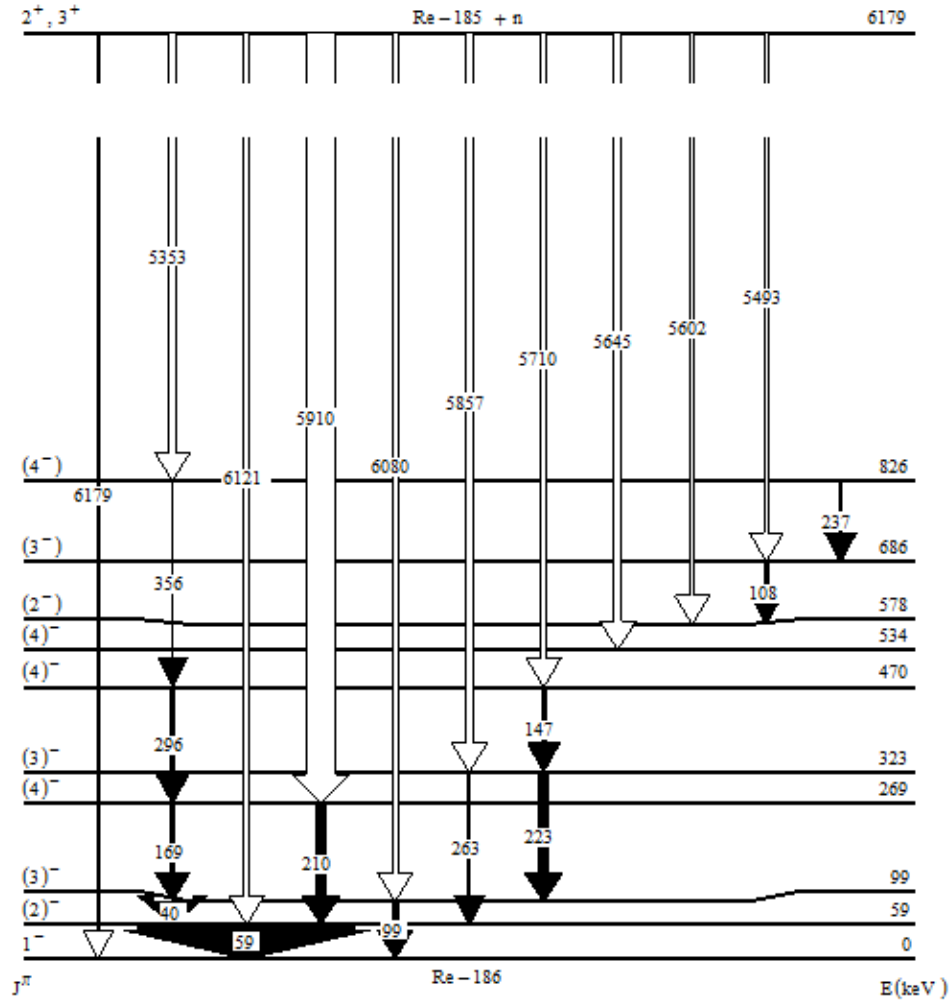


Figure 18. Population and depopulation of various energy levels below 865 keV resulting from select primary transitions. The thicknesses of the arrows signify gamma-ray intensities.

Table 3 contains the measured excitation energies, the excitation energies per literature, level spin-parity assignments, and depopulation gamma-ray attributes for all levels below 865 keV.

Table 3. The low-energy region decay scheme of ^{186}Re . The experimental energy levels were determined via the application of a linear least-squares fit. The literature values for the energy levels, spin-parity assignments, and multiplicities are from the ENSDF [2]. The cross sections are corrected for self absorption and abundance. Quantities in parentheses are uncertainties in significant figure format and quantities inside braces are proposals resulting from this work.

$E_{L\text{-exp.}}$ [keV]	ΔE [keV]	$E_{L\text{-lit.}}$ [keV]	J^π	E_γ [keV]	σ_γ [b]	α	XL
0.00	0	0	1^-				
59.05(1)	+0.04	59.010(3)	2^-	59.00(1)	13.29(94)	4.14(6)	M1
99.35(1)	-0.01	99.361 3	3^-	40.35(1)	2.35(19)	15.6(12)	M1+E2
				(99.36(4)) ^a	(0.48(5)) ^b	4.23(6)	E2
146.23(1)	-0.04	146.274 4	3^-	{46.72(15)}	{0.05(3)}	{8.23(14)}	{E2}
				87.23(1)	1.66(11)	7.65(11)	M1
				(146.27(1)) ^a	(0.13(3)) ^b	0.96(1)	E2
-	-	149 7	8^+	-			
173.92(1)	-0.01	173.929(4)	4^-	74.56(2)	0.88(5)	12.0(2)	M1+E2
-	-	≈ 186	6^-	-			
210.65(1)	-0.05	210.699(5)	2^-	(64.42(4)) ^a	(0.03(1)) ^b	15(12)	M1,E2
				(111.34(1)) ^a	(0.64(13)) ^b	3.80(6)	M1
				151.48(5)	1.28(8)	1.2(4)	E2+M1
				(210.69(2)) ^a	(1.50(24)) ^b	0.62(3)	M1+E2
268.78(1)	-0.02	268.798(6)	4^-	(122.53(1)) ^a	(1.20(32)) ^b	2.4(6)	M1,E2
				169.43(3)	0.24(3)	0.78(1)	E2+M1
				(209.82(2)) ^a	(0.24(8)) ^b	0.272(4)	E2
273.62(1)	-0.01	273.627(5)	4^-	(99.70(1)) ^a	(0.21(8)) ^b	4.8(6)	M1,E2
				127.30(4)	0.53(11)	1.84(23)	M1+E2
				(174.27(1)) ^a	(0.78(21)) ^b	0.74 12	M1+E2
313.84(1)	-0.16	314.009(5)	3^+	103.55(3)	0.45(3)	0.35(1)	E1
				(167.74(1)) ^a	(0.19(5)) ^b	0.10(0)	E1
				214.62(9)	2.41(48)	0.05(0)	E1
				255.00(2)	0.78(32)	0.04(0)	E1
316.37(2)	-0.09	316.463(12)	1^-	257.45(5)	0.86(13)	0.31(4)	M1+E2
				316.26(4)	1.31(8)	0.21(0)	M1
317.82(1)	-0.03	317.845(7)	5^-	(143.92(1)) ^a	1.15(24)	1.25(14)	M1+E2
				218.94(21)	0.05(3)	0.24(1)	E2
322.32(1)	-0.06	322.379(6)	3^-	(111.67(1)) ^a	(0.67(19)) ^b	3.3(6)	M1,E2
				(148.37(1)) ^a	(0.04(1)) ^b	1.3(4)	M1,E2
				(176.11(1)) ^a	(0.17(5)) ^b	0.8(3)	M1,E2
				(223.03(3)) ^a	(0.23(8)) ^b	0.38(4)	M1+E2
				263.26(6)	0.11(3)	0.24(11)	M1,E2

$E_{L-exp.}$ [keV]	ΔE [keV]	$E_{L-lit.}$ [keV]	J^π	E_γ [keV]	σ_γ [b]	α	XL
-	-	≈ 330	5^+	(144.15(1)) ^a	(2.51(11)) ^b	0.15(0)	E1
-	-	342(2)?		-			
351.06(2)	-0.14	351.202(16)	3^+	(204.96(15)) ^a	(0.05(3)) ^b	0.06(0)	E1
				251.81(3)	4.63(27)	0.04(0)	E1
378.35(2)	-0.04	378.392(12)	2^-	(61.93(4)) ^a	(1.15(19)) ^b	7(5)	M1+E2
				(232.10(2)) ^a	(0.56(8)) ^b	0.48(1)	M1
				319.40(4)	0.40(3)	0.14(7)	M1,E2
				378.42(5)	1.58(11)	0.13(0)	M1
417.77(1)	-0.02	417.792(8)	5^-	(144.15(5)) ^a	(0.32(11)) ^b	1.4(4)	M1,E2
				(148.99(1)) ^a	(0.32(11)) ^b	1.2(4)	M1+E2
				271.59(12)	0.13(3)	0.12(0)	E2
420.39(4)	-0.17	420.559(7)	4^+	106.55(4)	0.53(5)	3.5(3)	M1+E2
425.56(4)	-0.26	425.823(7)	$2^+, 3^+, 4^+$	111.81(4)	0.16(6)		
				{425.70(26)}	0.16(3)		
462.93(2)	-0.04	462.969(9)	5^-	(145.13(1)) ^a	(0.13(3)) ^b	1.4(4)	M1,E2
				189.25(2)	0.94(5)	0.62(23)	M1+E2
				(193.95(10)) ^a	(0.11(3)) ^b	0.59(23)	M1,E2
				289.44(20)	0.08(1)	0.18(9)	M1,E2
				363.45(5)	0.45(11)	0.05(1)	E2
469.74(1)	-0.04	469.779(17)	4^-	(147.42 (1)) ^a	(1.47(29)) ^b	1.3(4)	M1+E2
				201.00(3)	0.24(3)	0.51(20)	M1,E2
				(295.88(15)) ^a	0.19 5	0.25(1)	M1
470.50(2)	-0.01	470.514(13)	3^-	92.15(1)	0.48(3)	6.01(9)	M1+E2
				(148.09(6)) ^a	(0.03(1)) ^b	1.3(4)	M1,E2
				(201.78(10)) ^a	(0.03(1)) ^b		
				(411.18(20)) ^a	(0.27(5)) ^b		M1,E2
-	-	≈ 471	4^+	141.27(3)	0.32(5)	1.6(3)	M1+E2
497.29(4)	+0.00	497.293(10)	6^-	179.45(4)	0.21(3)	0.75(17)	M1,E2
500.57(1)	-0.18	500.722(16)	4^+	(149.52(1)) ^a	0.88(40)	1.06(11)	M1+E2
				401.21(1)	0.11(3)		E1
534.39(4)	+0.02	534.37(4)	4^-	(260.87(15)) ^a	(0.32(5)) ^b	0.24(11)	M1,E2
				360.44(4)	1.02(5)	0.14(0)	M1
548.98(6)	-0.35	549.330(9)	$+$	123.42(4)	0.29(3)	2.27(4)	M1+E2
559.78(4)	-0.20	559.976(9)	5^+	134.22(1)	0.08(1)		
				(139.42(1)) ^a	(0.19(3)) ^b	1.35(19)	M1+E2
-	-	≈ 562	6^+	232.05(4)	0.78(5)	0.48(1)	M1
577.65(2)	-0.07	577.723(16)	2^-	199.27(3)	0.37(3)	0.53(21)	M1,E2
				261.37(5)	0.91(19)	0.35(1)	M1

$E_{L-exp.}$ [keV]	ΔE [keV]	$E_{L-lit.}$ [keV]	J^π	E_γ [keV]	σ_γ [b]	α	$X L$
588.67(3)	-0.04	588.709(13)	4^-	118.18(2)	0.43(3)	2.7(6)	M1,E2
601.65(4)	+0.07	601.58(3)	1^+	285.16(4)	0.53(3)	0.03(0)	E1
				390.93(5)	3.40(24)	0.01(0)	E1
623.83(6)	-0.06	623.89(6)	1^-	(301.36(15)) ^a	(0.16(3)) ^b		
				413.21(6)	0.45(3)		
646.13(6)	-0.20	646.332(19)	5^-	176.35(6)	0.64(13)	0.8(3)	M1,E2
				(228.42(10)) ^a	(0.21(5)) ^b	0.35(15)	M1,E2
				(328.42(20)) ^a	(0.13(3)) ^b	0.13(6)	M1,E2
657.96(4)	-0.03	657.99(3)	2^+	(56.41(1)) ^a	(0.13(3)) ^b	29.7(5)	M1+E2
				335.67(13)	0.05(1)	0.02(0)	E1
				(341.38(20)) ^a	(0.13(5)) ^b	0.02(0)	E1
665.11(4)	-0.08	665.188(18)	5^+	164.54(3)	0.27(3)	0.89(7)	M1+E2
680.00(10)	-0.03	680.03(15)	$2^-,3^-$	357.68(5)	0.32(3)		
				(469.39(20)) ^a	(0.32(11)) ^b		
				(680.00(10)) ^a	(0.40(11)) ^b		
685.99(2)	-0.07	686.058(17)	3^-	(108.34(1)) ^a	(0.19(8)) ^b	3.6(6)	M1,E2
				(215.28(15)) ^a	(0.11(5)) ^b	0.42(7)	M1,E2
				307.66(4)	0.75(8)	0.22(0)	M1
-	-	689.3	1^-	-			
691.38(6)	+0.04	691.34(15)	6^-	(193.95(10)) ^a	0.08(3)	0.57(22)	M1,E2
				(228.42(10)) ^a	0.08(3)	0.35(15)	M1,E2
				373.63(7)	0.08(1)	0.09(5)	M1,E2
736.07(4)	-0.06	736.127(15)	5^-	147.40(2)	1.18(8)	1.3(4)	M1,E2
744.50(46)	-0.31	744.81(5)	3^+	86.45(24)	0.00(0)		
				{744.50(46)}	{0.19(8)}		{E2}
761.45(15)	+0.03	761.42(19)	$1^-,2^-,3^-$	438.91(21)	0.16(3)		
				551.30(26)	0.40(5)		
				760.88(38)	0.24(3)		
785.13(6)	-0.18	785.31(20)		406.77(6)	0.21(3)		
				469.42(22)	0.19(5)		
				{785.09(39)}	{0.08(3)}		
791.34(16)	-0.16	791.5	1^-	-			
796.14(7)	-0.49	796.63(20)	≤ 3	218.27(10)	0.11(1)		
				418.30(19)	0.29(3)		
				479.70(22)	0.88(8)		
				584.34(31)	0.48(5)		
				796.22(46)	0.16(8)		
-	-	803(10)		-			

$E_{L-exp.}$ [keV]	ΔE [keV]	$E_{L-lit.}$ [keV]	J^π	E_γ [keV]	σ_γ [b]	α	XL
-	-	812.2	1 ⁻	-			
819.22(10)	+0.28	818.94(19)	2 ^{-,3-}	496.94(25)	0.35(8)		
				607.58(29)	0.65(8)		
				645.72(31)	0.35(5)		
				760.88(38)	0.24(3)		
				{819.95(42)}	{0.08(3)}		
821.34(5)	+0.03	821.31(6)	≤ 3	(163.31(6)) ^a	(0.08(3)) ^b		
				219.83(5)	0.16(1)		
826.09(4)	-0.06	826.152(18)	4 ⁻	140.07(3)	0.67(11)	1.5(5)	E2,M1
				(237.60(15)) ^a	(0.11(3)) ^b	0.32(14)	M1,E2
				(355.63(5)) ^a	(0.29(3)) ^b	0.10(5)	M1,E2
854.97(14)	-0.07	855.04(5)	4 ⁺	(110.24(9)) ^a	(0.37(5)) ^b	3.4(6)	M1,E2
				196.90(17)	0.05(1)	0.34(1)	E2
-	-	857.9	2 ^{-,3-}	-			
863.37(7)	-0.80	864.17(15)	2 ^{-,3-}	286.41(8)	0.13(1)		

^aMultiplet or unobserved transition resolved using ENSDF branching ratios [2].

^bIntensity normalized to ENSDF-reported branching ratios [2].

Table 4 is a comparison of the measured relative depopulation intensities associated with the first 15 excited states, except for the 149-keV and 186-keV levels (no depopulation transitions were observed), to the ENSDF-adopted relative intensities.

Table 4. Level relative intensity comparison for the first 15 excited states. Literature values are from the ENSDF [2]. The cross sections are corrected for self absorption and abundance. Quantities in parentheses are uncertainties in significant figure format and quantities inside braces are proposals resulting from this work.

$E_{L-exp.}$ [keV]	$E_{\gamma-exp.}$ [keV]	$E_{\gamma-lit.}$ [keV]	$\sigma_{\gamma-exp.}$ [b]	Relative $I_{\gamma-exp.}$	ΔI_γ	$I_{\gamma-lit.}$
0	-	-				
59.05(1)	59.00(1)	59.009(4)	13.29(94)	100.0	0.0	100.0
99.35(1)	40.35(1)	40.350(3)	2.35(19)	100.0	0.0	100.0
	99.36(4)	99.362(4)	0.48(5)	20.4	-0.9	21.3
146.23(1)	{46.72(15)}	-	{0.05(3)}	{3.0}	-	-
146.23(1)	{46.72(15)}	-	{0.05(3)}	{3.0}	-	-
	87.23(1)	87.266(4)	1.66(11)	100.0	0.0	100.0
173.92(1)	74.56(2)	74.568(3)	0.88(5)	100.0	0.0	100.0
210.70(6)	64.42(4)	64.42(4)	0.03(1)	2.0	+0.3	1.7

$E_{L-exp.}$ [keV]	$E_{\gamma-exp.}$ [keV]	$E_{\gamma-lit.}$ [keV]	$\sigma_{\gamma-exp.}$ [b]	Relative $I_{\gamma-exp.}$	ΔI_{γ}	$I_{\gamma-lit.}$
	111.34(1)	111.337(8)	0.64(13)	42.7	+0.7	42.0
	151.48(5)	151.686(5)	1.28(8)	85.3	+0.3	85.0
	210.69(2)	210.685(17)	1.50(24)	100.0	0.0	100.0
268.78(1)	122.53(1)	122.525(5)	1.20(32)	100.0	0.0	100.0
	169.43(3)	169.431(8)	0.24(3)	20.0	0	20.0
	209.82(2)	209.82(2)	0.24(8)	20.0	-1.0	21.0
273.62(1)	99.70(1)	99.696(4)	0.21(2)	26.9	-0.1	27.0
	127.30(4)	127.352(4)	0.53(2)	67.9	-1.1	69.0
	174.27(1)	174.271(9)	0.78(4)	100.0	0.0	100.0
313.84(1)	103.55(3)	103.310(6)	0.45(3)	18.7	-0.3	19.0
	167.74(1)	167.737(8)	0.19(5)	7.8	+0.4	7.4
	214.62(2)	214.648(8)	2.41(48)	100.0	0.0	100.0
	255.00(2)	254.995(15)	0.78(32)	{32.4}	-21.6	(54.0) ^a
316.37(2)	257.45(5)	257.446(15)	0.86(13)	{65.6}	+9.6	(56.0) ^a
	316.26(4)	316.473(20)	1.31(8)	100.0	0.0	100.0
317.82(1)	143.92(1)	143.919(5)	1.15(24)	100.0	0.0	100.0
	218.94(21)	218.69(10)	0.05(3)	4.3	-0.3	4.6
322.32(1)	111.67(1)	111.674(6)	0.67(19)	100.0	0.0	100.0
	148.37(1)	148.37(6)	0.03(1)	4.5	-1.1	5.6
	176.11(8)	176.112(8)	0.19(5)	28.4	+2.4	26.0
	223.03(3)	223.035(15)	0.24(8)	35.8	+1.8	34.0
	263.33(20)	263.33(20)	0.11(3)	16.4	+0.4	16.0
351.06(2)	204.96(15)	204.96(15)	0.05(3)	1.1	-0.2	1.3
	251.81(3)	251.841(15)	4.63(27)	100.0	0.0	100.0
378.35(2)	61.93(4)	61.928(4)	1.15(19)	72.7	-0.3	73.0
	232.10(2)	232.100(16)	0.56(8)	35.4	+0.4	35.0
	319.40(4)	319.44(10)	0.40(3)	25.3	-0.7	26.0
	378.42(5)	378.42(5)	1.58(11)	100.0	0.0	100.0
417.77(1)	144.15(1)	144.152(5)	0.32(11)	100.0	+3.0	103.0
	148.99(1)	148.994(5)	0.32(11)	100.0	0.0	100.0
	271.59(12)	271.47(10)	0.13(3)	40.6	+0.6	40.0
420.39(4)	106.55(4)	106.550(4)	0.53(5)	100.0	0.0	100.0

^aStatistical-model calculations indicate that the ENSDF branching ratio may be in error [2].

Table 4 displays two proposed branching ratio amendments, one each for the 313.84(1)-keV and 316.37(2)-keV levels, which were revealed via statistical modeling. An absolute intensity balance for the same levels is offered in Table 5.

Table 5. Level absolute intensity comparison for the first 15 excited states. The cross sections are corrected for self absorption and abundance. Quantities in parentheses are uncertainties in significant figure format.

$E_{L-exp.}$ [keV]	$\Sigma\sigma_{\gamma-In}$ [b]	$\Sigma\sigma_{\gamma-Out}$ [b]	$\Sigma\sigma_{\gamma-Net}$ [b]
59.05(1)	60(5)	68(5)	8(7)
99.35(1)	25.4(12)	42(5)	16(5)
146.23(1)	7.8(15)	15.1(11)	7.3(18)
173.92(1)	5.9(8)	11.4(7)	7.3(18)
210.70(6)	9.3(10)	8.8(10)	-0.5(14)
268.78(1)	3.0(6)	4.8(14)	1.9(15)
273.62(1)	2.7(4)	4.1(7)	1.3(8)
313.84(1)	2.5(4)	4.2(6)	1.6(7)
316.37(2)	12(5)	2.71(20)	-9(6)
317.82(1)	0.91(12)	2.6(6)	1.7(6)
322.32(1)	1.99(18)	2.9(7)	0.9(7)
351.06(2)	1.8(9)	4.9(3)	3.1(9)
378.35(2)	5.4(3)	12(6)	7(6)
417.77(1)	0.28(8)	1.6(7)	1.3(7)
420.39(4)	0.45(8)	2.4(3)	1.9(3)

This table indicates that 14 of the first 15 excited states experience more depopulation than population within the limits of uncertainty. The level at 316.37(2) keV exhibited significant overpopulation with a high level of uncertainty, which is attributed to a 61.93(4)-keV transition from the 378.35(2)-keV level. The 378.35(2)-keV level shows a commensurate over depopulation and high level of uncertainty. The high uncertainties are due to the fact that the multipole mixing ratio of the 61.93(4)-keV transition is not well known, thereby affecting the degree to which the cross section is corrected for internal conversion.

4.4 Statistical Model Calculations

Preliminary statistical modeling was conducted with DICEBOX, whereby the critical energy E_{crit} was set at 323 keV such that the measured depopulations of the first

11 observed excited states were considered in the simulations. The intensity balance displayed in Table 3 indicates that these level depopulation measurements are in reasonable accordance with ENSDF-adopted values and suitable for modeling purposes. Given that two LD models and two giant dipole electric resonance (GDER) PSF were considered in this work, there were four possible combinations examined: the constant temperature formula (CTF) LD with the Brink-Axel (BA) PSF, CTF LD with the enhanced generalized Lorentzian (EGLO) PSF, the back-shifted Fermi gas (BSFG) LD with the BA PSF, and the BSFG LD with the EGLO PSF. Table 6 and Table 7 give the LDM and PSF parameterization, respectively.

Table 6. Level density parameters associated with the CTF (T and E_0) and the BSFG formula (a and E_1), pairing energy (Δ), and average resonance spacing (D_0) used in the DICEBOX simulations. These values were obtained from Reference [23].

T [MeV]	E_0 [MeV]	a [MeV ⁻¹]	E_1 [MeV]	Δ [MeV]	D_0 [eV]
0.56(1)	-1.76(18)	19.87(28)	-0.90(10)	0.74(6)	3.1(3)

Table 7. Lorentz GDER and GQER resonance parameters used in the DICEBOX simulations. The values are those corresponding to natural rhenium from Reference [37]. For the GDER model, $G1$ accounts for the isovector vibration parameters along the axis of symmetry, while $G2$ are for those that are perpendicular to the symmetrical axis. The GQER parameters are associated with isovector-isoscalar vibrations.

Resonance	E_{G1} [MeV]	Γ_{G1} [MeV]	σ_{G1} [mb]	E_{G2} [MeV]	Γ_{G2} [MeV]	σ_{G2} [mb]
GDER	12.63	2.77	279.0	15.24	4.69	375.0
GQER	11.04	3.88	4.64	-	-	-

Within any combinations involving EGLO GDER PSF, a subset of simulations was conducted in which the enhancement factor k_0 was varied in order to ascertain the value that best represented the data and another subset was executed to determine the best

setting for the giant dipole magnetic resonance (GDMR) PSF single-particle strength $f_{SP}^{(M1)}$. These additional simulations revealed that $k_0 = 4.0$ for the CTF LDM, $k_0 = 3.0$ for the BSFG LDM, and $f_{SP}^{(M1)} = 3\text{e-}09 \text{ MeV}^{-3}$ were the most appropriate settings.

Additionally, per Reference [38], it was determined that the capture-state cross section corresponding to $J^\pi = 2^+$ and $J^\pi = 3^+$ is 0.474 and 0.526, respectively.

Following preliminary modeling based on σ_γ measurements for ^{186}Re , a comparison of the four combinations is exhibited in Figure 19. Each data point represents an energy level. The upper plots show the levels classified by spin, while the bottom plots categorize them by their parities. Based on the number of levels that fall upon the diagonal line within their respective uncertainties, the combination of BSFG and EGLO emerges as most representative of the data. Under this combination, all 11 data points fall along the diagonal within their respective uncertainties. This combination yields a capture state total radiative width Γ_0 of 51(1) meV. This quantity was found to vary significantly with LD/PSF combination. It is within two standard deviations of the recommended value of 56(3) meV [38]. The degree of agreement exhibited in the comparison signifies that the measured cross sections are plausible, thereby reducing the possibility that the measurements themselves are responsible for any discrepancies observed during the statistical modeling process.

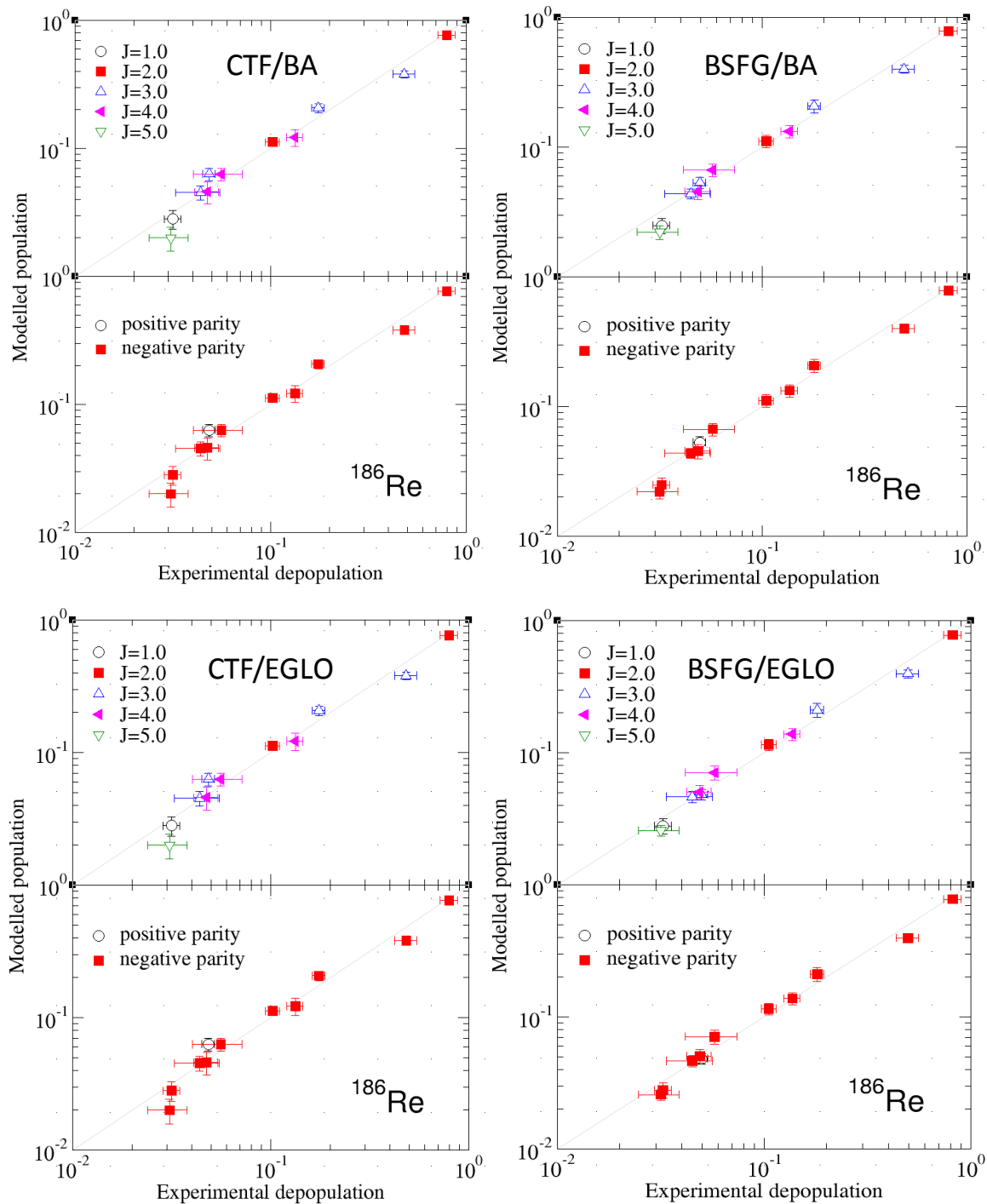


Figure 19. Comparison of various combinations of LD and GDER PSF. The combination that best reproduced the data was assigned as the most likely to represent the structure of ^{186}Re . For each of the four scenarios, the upper chart shows the energy levels, represented by the data points, per their respective spins and the lower chart differentiates them by parity.

The results further indicate that the statistical modeling process is incomplete and further simulation is required to validate the measurements contained in this work.

4.5 Energy Levels of Interest

4.5.1 1^- Ground State

With consideration given to the ground-state spins of the nearest isotopes and isotones (i.e. nuclei that possess the same number of neutrons but different number of protons), the orbital configurations of the ^{186}Re unpaired proton and neutron are such that $J^\pi = 1^-$ is the most likely spin-parity assignment [14]. Additionally, the $5/2^+$ spin-parity of the ^{185}Re target nucleus enables a $J^\pi = 2^+$ and/or 3^+ spin-parity assignment for the capture state [39]. Due to the fact that $E1$ is the most likely multipole for primary transitions from the capture state, the selection rules indicate that the primary to ground state transition is likely from a $J^\pi = 2^+$ parent state. The theoretical spin-parity assignments are supported by measurements in this work and others [1, 13, 14].

4.5.2 2^- Level at 59 keV

The 59.05(1)-keV level is established via the most intense transition observed in this work, which was a 59.00(1)-keV gamma ray that populates the ground state with a σ_γ of 13.29(94) b. Previous work suggests that the spin of this level is determined by conversion electron data because of the angular distribution of the proton groups. The electron data indicates that the parity of this level must be negative and that $I = 0, 1$, or 2 [14]. Per the selection rules, if 0^- was the case, then the primary transition populating this level is an $M2$, which is clearly inconsistent with the observed intensity of that transition. Due to the fact that the ground state's known spin-parity is 1^- and that the next level to

possess this state is predicted at excitation energies sufficiently above 59 keV, $J^\pi = 1^-$ is also highly unlikely for the 59-keV level [14]. Therefore, the most likely assignment for this level is $J^\pi = 2^-$, which means that the observed 59.0-keV gamma-ray multipole is $M1$ as mandated by the selection rules. This multipole assignment is compatible with the measured intensity of the transition and the spin-parity assignment is consistent with the measured 6120.51(8) keV $E1$ -primary transition from the capture state. The measured depopulation of this level is in agreement with the simulated population given by DICEBOX as displayed in Figure 19. Also, previous measurements compare well with the attributes assigned to the level in this work.

4.5.3 3^- Level at 99 keV

The multipolarity assignments of the transitions depopulating the 99.35(1)-keV level, which are a 40.35(1) keV transition and a ground-state transition, are taken from Reference [2]. The multipoles indicate that the parity of this level is negative and it can take spin values of 1, 2, or 3 assuming $J^\pi = 2^-$ is the correct assignment for the 59.05(1)-keV level. The spin assignments of 1 or 2 are not likely because they would require the $M1$ component of the 99.36(4)-keV transition to be very small compared with the $E2$ component [14]. However, the 40.35(1)-keV line has a very small mixture of $E2$ relative to its $M1$ component, which implies that the $M1$ component is sufficiently strong such that a spin assignment of 1 or 2 is not likely. Therefore, the spin-parity assignment is most probably 3^- , thus satisfying both conditions. Additionally, this characterization is well-suited for the observed 6080.14(8)-keV primary transition from the capture state. Moreover, this excited state is an isomer with a half-life of 25.5(25) ns [2]. As with its

lower lying neighbor, DICEBOX calculations for the 99.35(1)-keV level compare well with the measured experimental data in this work as demonstrated in Figure 19.

4.5.4 3^- Level at 146 keV

The known multipolarity of the 87.23(1)-keV line depopulating the 146.23(1)-keV level is $M1$ [2]. Moreover, the spin of its destination level indicates that the spin-parity of the 146.23(1)-keV level is 3^- . The other depopulating transition is a ground state transition. Therefore, the selection rules with respect to a transition from a $J^\pi = 3^-$ to a $J^\pi = 1^-$ state imply that the 146.27(1)-keV transition is an $E2$. This assignment is also plausible considering the measured 6032.87(13)-keV primary transition from a 2^+ capture state. Furthermore, the DICEBOX results in Figure 19 suggest that the characteristics assigned to this level are very reasonable.

4.5.5 8^+ Level at 149 keV

This level is the metastable-excited state with a half-life of 200,000 years and it is thought to exist at 149(7) keV with a $J^\pi = 8^+$ [2]. The relatively large uncertainty in energy is due to very little experimental evidence of what populates and depopulates the level. In Reference [1], it is proposed that the level is depopulated by a ≈ 50 keV $E5$ -transition to the level at 99 keV based on a low-resolution, high-geometry, conversion-electron spectrum. Given the half-life of this level and the multipolarity of the gamma ray, its observation was not expected in this work nor was it seen. It was also proposed, as shown in Figure 4, that the isomer is formed in approximately 0.3% of neutron captures by a ≈ 36 -keV transition from the 186-keV level [1]. The spin-parity of the 186-keV level is 6^- and thus the multipole of the gamma ray is likely an $E2$. There was a lack of compelling evidence for this transition because it is beneath the HPGe threshold.

Furthermore, this level is not considered in the DICEBOX calculations because there is no measured depopulation.

4.5.6 4^- Level at 174 keV

Evidence for the 173.92(1)-keV level is given by its sole depopulation gamma ray, which is measured at 74.56(2) keV and it feeds the 99.35(1)-keV level. The measured multipole of this transition is an $M1$ -heavy mixture with $E2$, thus the likely spin-parity of this level is 4^- [2]. The measured gamma ray resulting from a primary transition from a $J^\pi = 3^+$ capture state of energy 6005.45(12) keV provides further support for this assignment. The DICEBOX simulations support the experimental assignment per Figure 19.

4.5.7 6^- Level at 186 keV

As a result of the uncertainty in energy of the 149 keV metastable-excited state, the exact energy of the 186-keV level is also unknown. It is postulated that its modes of de-excitation are via a ≈ 11 -keV gamma ray to the 174-keV state and a ≈ 36 -keV gamma ray to the metastable state, neither of which were observed in this work [1]. Therefore, there are no means by which to accurately place this level. However, the level is populated by a 144.15(1)-keV gamma ray that is an $E1$ from the 330-keV state with $J^\pi = 5^+$, signifying that this level possesses a spin-parity of 4^- or 6^- . An $E2$ is the most likely transition to the $J^\pi = 8^+$ metastable state, therefore $J^\pi = 6^-$ is the most probable spin of the 186-keV level. For the same reason given for the metastable-excited state, this level does not factor into the DICEBOX computations. However, assuming that there is only one depopulation transition, it can be argued that the depopulation intensity of the 186-keV is equivalent to the intensity of the 144.15(1)-keV gamma ray that feeds it.

4.5.8 2^- Level at 211 keV

This level at 210.65(1) keV is confirmed by means of the 151.48(5)-keV gamma ray, which depopulates it, and the 59.05(1)-keV energy level. There are two additional depopulation transitions at 111.34(1) keV and 210.69(2) keV to the 99.35(1)-keV level and the ground state, respectively. The multipoles of the depopulating gamma rays consist of $M1$ and/or $E2$ [2]. Additionally, the destination levels possess tentative spin-parities of 1^- , 2^- , and 3^- . Given the measured multipoles, $J^\pi = 2^-$ is most likely for the 210.65(1)-keV level. This is representative of the exception to the angular momentum selection rule, where $I_i = I_f$. Since the selection rules state L cannot equal zero, any transitions between an initial and final state with equivalent I is a dipole. The assignment is also supported by a measured 5968.79(16)-keV primary transition from the capture state. This level is also an isomer with a half-life of less than 0.2 ns [2]. Figure 19 reveals that the DICEBOX simulations are consistent with the experimental measurements.

4.5.9 4^- Level at 269 keV

The 268.78(1)-keV level was ascertained through the observation of the 122.53(1)-keV gamma ray and its 146.23(1)-keV destination level. The other two branches for depopulation are a 169.43(3)-keV gamma ray to the 99.35(1)-keV state and a 209.82(2)-keV gamma ray to the 59.05(1)-keV state. The tentatively assigned multipoles associated with this level are $M1$ and/or $E2$, thus the 268.78(1)-keV level is likely to have a $J^\pi = 4^-$ because of the 2^- and 3^- spin-parity assignments of the depopulation transitions' destination levels. This level is populated, at least in part, by the most intense primary transition, which has an energy of 5910.60(8) keV and the σ_γ is

1.66(11) b. Relative to most other primary transitions, this σ_γ is higher by one order of magnitude. The transition is most likely an $E1$ from a 3^+ capture state. The accuracy of this level's characterization is brought out by the DICEBOX simulations as shown in Figure 19.

4.5.10 4^- Level at 274 keV

A level at 273.62(1) keV was determined via its 127.30(4)-keV gamma ray and the 146.23(1)-keV level. The other known transitions out of this level are 99.70(1)-keV and 174.27(1)-keV gamma rays to the 173.92(1)-keV and 99.35(1)-keV levels, respectively. The multipoles of the depopulation transitions are mixtures of $M1$ and $E2$. The spin-parity assignments of the destination levels are 3^- or 4^- . There is also a measured gamma ray with energy of 5905.44(2) keV due to a primary transition from the capture state. Therefore, the most likely spin-parity of the 273.62(1)-keV level is 4^- , which is supported by the DICEBOX results depicted by Figure 19.

4.5.11 3^+ Level at 314 keV

The 210.65(1)-keV level and a 103.55(3)-keV gamma ray implies a parent level at 313.84(1) keV. There are three additional transitions from this level: 167.74(1)-keV, 214.62(2)-keV, and 255.00(2)-keV gamma rays to the 146.23(1)-keV, 99.35(1)-keV, and 59.05(1)-keV levels, respectively. The multipoles of the transitions from this level are all of the $E1$ type. Furthermore, the destination levels possess spin-parities of 2^- or 3^- . Therefore, the assignment for this level is most likely $J^\pi = 2^+$ or 3^+ . A primary transition to this level was not observed, which is understandable considering $E1$ multipoles are dominant from the capture state. Reference [2] has given a tentative assignment of $J^\pi =$

3^+ , which is sustained by the DICEBOX simulations in Figure 19. This level is an isomer with a half-life of 24.1(11) ns [2].

4.5.12 1^- Level at 316 keV

The position of this level is established at 316.37(2) keV by observation of two known depopulation transitions: a 257.45(5)-keV gamma ray to the 59.05(1)-keV level and a 316.26(4)-keV gamma ray to the ground state. The measured gamma-ray multipoles are $M1 + E2$ (257.45(5) keV) and $M1$ (316.26(4) keV) and the destination level spin-parities are 1^- and 2^- , meaning the 316.37(2)-keV level likely possesses a $J^\pi = 1^-$ assignment. This level is also populated by a 5862.55(42)-keV primary from the capture state. As with the previous level, the DICEBOX calculations displayed in Figure 19 predict that the assignments associated with this level are plausible. Also like the previous level, it is an isomer with a half-life of 0.2(1) ns [2].

4.5.13 5^- Level at 318 keV

This level is situated at 317.82(1) keV as established by its 143.92(1)-keV depopulation transition and the 173.92(1)-keV level. The other depopulation transition belonging to this level is 218.94(21) keV to the 99.35(1) keV level. The measured multipole for the 143.92(1)-keV transition is a mixed $M1+E2$ [2]. The J^π of its destination level is 4^- , which indicates that the likely assignment for the 317.82(1)-keV level is $J^\pi = 3^-, 4^-, \text{ or } 5^-$. A primary transition to this level was not observed, which implies that $J^\pi = 5^-$ for this state. As evidenced by Figure 19, the DICEBOX simulations support the experimental data.

4.5.14 3^- Level at 322 keV

The position of the 322.32(1)-keV level is supported by the five depopulation transitions assigned to it at 111.67(1), 148.37(1), 176.11(8), 223.03(3), and 263.33(20) keV. The level is allocated a J^π of 3^- and the depopulation transitions are either $M1$, $E2$, or a mixture of the two because the parities of the destination levels are all negative. What is more, the spin of both the 99.35(1)-keV and the 146.23(1)-keV levels is also 3. Therefore, the exception to the angular momentum selection rule mandates the transitions to these two levels are most likely characterized by an $M1$ assignment. The measured 5857.03(9) keV $E1$ -primary transition from the capture state is consistent with this assignment. The DICEBOX calculations show agreement with this assessment per Figure 19.

4.5.15 5^+ Level at 330 keV

This level is purported to be in the vicinity of 330 keV. There is one depopulating transition ascribed to this level. However, its destination level, around 186 keV, is also poorly known, making a more precise measurement of the 330 keV-level very difficult. Nonetheless, the known multipolarity of this gamma ray is $E1$ and the J^π of the 186 keV level is 6^- , which suggests a likely spin-parity assignment of 5^+ or 7^+ . $J^\pi = 5^+$ is more probable, however, as lower order multipoles are more common than higher ones. The selection rules make a primary transition from the capture state unlikely and one was not observed in this work. Furthermore, this level is an isomer with a half-life of 17.3(6) ns [2].

4.5.16 3^+ Level at 351 keV

Determination of the 351.06(2)-keV level resulted from its 204.96(15) and 251.81(3)-keV transitions to the 99.35(1) and the 146.23(1)-keV level, respectively. The spin-parity assignment for this level is 3^+ . The measured multipolarity of the 251.81(3)-keV gamma ray is $E1$ and that of the 204.99(13)-keV gamma ray is likewise tentatively assigned as $E1$. The J^π of both destination levels is 3^- . Per the selection rules, since the parity changes, these transitions are, indeed, very likely $E1$. This assignment is also supported by the fact that no primary transitions to this level were observed. Additionally, this level is an isomer with a half-life of less than 0.2 ns [2].

4.5.17 2^- Level at 378 keV

The 378.35(2)-keV levels was ascertained via four depopulation transitions at 61.93(4), 232.10(2), 319.40(4), and 378.42(5) keV, which, along with the observed 5800.81(22)-keV primary transition, lend verification to its placement. The 61.93(4)-keV and the 378.42(5)-keV gamma rays are both $M1$, while it is assumed that the 61.93(4) keV gamma ray possesses a small mixture of $E2$ [2]. The destination levels of these transitions are 316.26(4) keV and the ground state, respectively. Both of these states possesses a J^π of 1^- , which supports a tentative $J^\pi = 2^-$ assignment for the 378.35(2)-keV level. This designation also conforms to a 5800.81(12) keV $E1$ -primary transition from the capture state.

4.5.18 5^- Level at 418 keV

This energy level at 417.77(1) keV was deduced on the basis of three depopulation transitions of 144.15(1), 148.99(1) and 271.59(12) keV to the 273.62(1)-keV, 268.78(1)-keV, and the 146.23(1)-keV levels, which offers strong evidence for this

level's existence. The spin-parity assignment of this level is likely 5^- [2]. Of the three transitions, the multipole of the 148.99(1)-keV gamma ray is known and it is a mixed $M1 + E2$. Its destination is the 268.78(1)-keV level with $J^\pi = 4^-$, which is consistent with an $M1$ transition. Additionally, no primary transition to this level was observed, which is expected for a level has $J^\pi = 5^-$.

4.5.19 4^+ Level at 420 keV

The 420.39(4)-keV level is predicated on a 106.55(4)-keV transition to the level at 313.84(1) keV. The combination of the observed gamma-ray lines at 106.55(4) keV and the 5759.25(4) keV, which results from a primary transition, gives credence to its placement. The multipolarity of the 106.55(4) keV line is mixed $M1$ and $E2$. The J^π of its destination level is 3^+ , thus the likely spin-parity of the 420.39(4)-keV level is 3^+ or 4^+ . Reference [2] tentatively gives $J^\pi = 4^+$ as the assignment.

4.5.20 Summary of Energy Level Measurements

Table 8 is a comparison of energy level measurements in this work to previous data sets.

Table 8. Summary of energy level measurements. Quantities in parentheses are uncertainties in significant figure format.

This Work	R. G. Lanier [14]	C. Wheldon [13]	C. M. Baglin [2]
E_L [keV]	E_L [keV]	E_L [keV]	E_L [keV]
59.05(1)	59.009(4)	59.0(5)	59.010(3)
99.35(1)	99.361(3)	99.6(5)	99.361(3)
146.23(1)	146.275(6)	146.7(5)	146.274(4)
173.92(1)	173.929(6)	173.9(5)	173.929(4)
210.65(1)	210.696(6)	210.5(5)	210.699(5)
268.78(1)	268.796 (11)	268.8(5)	268.798(5)
273.62(1)	273.628(5)	273.5(5)	273.627(5)
313.84(1)	314.009 (7)	-	314.009(5)
316.37(2)	316.463 (12)	317.4(5)	316.463(12)

This Work	R. G. Lanier [14]	C. Wheldon [13]	C. M. Baglin [2]
E_L [keV]	E_L [keV]	E_L [keV]	E_L [keV]
317.82(1)	-	-	317.845(7)
322.32(1)	322.391(7)	322.4(5)	322.379(6)
351.06(2)	-	-	351.202(16)
378.35(2)	378.383(11)	378.6(5)	378.392(12)
417.77(1)	417.790(12)	418.7(5)	417.792(8)
420.39(4)	-	-	420.559(7)

Table 8 demonstrates that the measurements made in this work are consistent with previous works. It should be noted that Reference [2] is the ENSDF nuclear data sheet, which is an evaluated compilation of multiple data sets. It appears that this data sheet heavily favored the data set represented by Reference [14]. Lastly, this work was able to measure energy levels that were not identified in the References [13] and [14]. This can likely be attributed to the high enrichment of the sample, the Compton-suppressed spectrometer and the low level of background radiation in the test chamber.

4.6 Neutron Separation Energy for ^{185}Re

The measured primary transitions, both those previously known and those newly identified in this work, were used to calculate an independent measurement of the neutron-separation energy S_n . The separation energy as computed for each primary transition $S_{n,i}$ is defined as

$$S_{n,i} = E_{\gamma,i} + E_{Exc,i} + T_{R,i}, \quad (31)$$

where $E_{\gamma,i}$ is the gamma-ray energy of primary transition i , $E_{Exc,i}$ is the associated excitation energy, and $T_{R,i}$ is the corresponding kinetic energy of the nucleus recoil. This work calculated the separation energy via two methods. The first method consisted of

adding each recoil-corrected primary transition to the corresponding ENSDF-adopted destination level $E_{L-lit.}$ per

$$S_{n,i} = E_{\gamma,i} + E_{L-lit.,i} + T_{R,i}. \quad (32)$$

The second method involved adding each recoil-corrected primary transition to energy levels measured in this work $E_{L-exp.}$ as shown by

$$S_{n,i} = E_{\gamma,i} + E_{L-exp.,i} + T_{R,i}. \quad (33)$$

The calculation was performed for primary transitions that populate levels below 865 keV. The uncertainty associated with levels above this benchmark is such that including them in the calculation is not useful. Table 9 is $S_{n,i}$ calculated with the adopted levels.

Table 9. Neutron-separation energies calculated with the ENSDF-adopted levels [2]. Quantities in parentheses are uncertainties in significant figure format and braces are proposals resulting from this work.

E_{γ} [keV]	$E_{L-lit.}$ [keV]	T_R [keV]	S_n [keV]
6179.22(15)	0	0.11	6179.33(15)
6120.51(8)	59.010(3)	0.11	6179.63(8)
6080.14(8)	99.361(3)	0.11	6179.61(8)
6032.87(13)	146.274(4)	0.11	6179.25(13)
6005.45(12)	173.929(4)	0.10	6179.48(12)
5968.79(16)	210.699(5)	0.10	6179.59(16)
5910.60(8)	268.798(6)	0.10	6179.50(8)
{5905.44(20)}	273.627(5)	0.10	6179.17(20)
{5862.55(42)}	316.463(12)	0.10	6179.11(42)
5857.03(9)	322.379(6)	0.10	6179.51(9)
5800.81(12)	378.392(12)	0.10	6179.30(12)
5759.25(41)	420.559(7)	0.10	6179.90(41)
{5754.52(7)}	425.823(7)	0.10	6180.44(7)
5709.56(11)	469.779(17)	0.09	6179.43(11)
{5678.68(30)}	500.722(16)	0.09	6179.50(30)

E_γ [keV]	$E_{L-lit.}$ [keV]	T_R [keV]	S_n [keV]
5644.96(11)	534.37(4)	0.09	6179.42(12)
{5619.06(107)}	559.976(9)	0.09	6179.13(107)
5601.63(10)	577.723(16)	0.09	6179.44(10)
5493.41(8)	686.058(17)	0.09	6179.56(8)
{5416.80(89)}	761.42(19)	0.08	6178.30(91)
{5395.80(37)}	785.31(20)	0.08	6181.19(42)
5383.16(10)	796.63(20)	0.08	6179.87(22)
5360.33(12)	818.94(19)	0.08	6179.35(22)
5353.25(11)	826.152(18)	0.08	6179.48(11)
{5323.31(37)}	855.04(5)	0.08	6178.43(37)
5317.03(9)	864.17(15)	0.08	6181.28(17)

The arithmetic mean of all calculated $S_{n,i}$ was 6179.55(24) keV. The uncertainty associated with each separation energy calculation $\mu_{S_{n,i}}$ was determined via quadrature summing. The uncertainty in T_R was regarded as negligible. Table 10 is $S_{n,i}$ calculated with the experimentally determined levels.

Table 10. Neutron-separation energies calculated with the experimentally determined levels. Quantities in parentheses are uncertainties in significant figure format and braces are proposals resulting from this work.

E_γ [keV]	$E_{L-exp.}$ [keV]	T_R [keV]	S_n [keV]
6179.22(15)	0.00	0.11	6179.33(15)
6120.51(8)	59.05(1)	0.11	6179.67(8)
6080.14(8)	99.35(1)	0.11	6179.60(8)
6032.87(13)	146.23(1)	0.11	6179.21(13)
6005.45(12)	173.92(1)	0.10	6179.47(12)
5968.79(16)	210.65(1)	0.10	6179.54(16)
5910.60(8)	268.78(1)	0.10	6179.48(8)
{5905.44(20)}	273.62(1)	0.10	6179.16(20)
{5862.55(42)}	316.37(2)	0.10	6179.02(42)
5857.03(9)	322.32(1)	0.10	6179.45(9)
5800.81(12)	378.35(2)	0.10	6179.26(12)
5759.25(41)	420.39(4)	0.10	6179.74(41)
{5754.52(7)}	425.56(4)	0.10	6180.18(8)
5709.56(11)	469.74(1)	0.09	6179.39(11)

E_γ [keV]	$E_{L-exp.}$ [keV]	T_R [keV]	S_n [keV]
{5678.68(30)}	500.57(1)	0.09	6179.34(30)
5644.96(11)	534.39(4)	0.09	6179.44(12)
{5619.06(107)}	559.78(4)	0.09	6178.93(107)
5601.63(10)	577.65(2)	0.09	6179.37(10)
5493.41(8)	685.99(2)	0.09	6179.49(8)
{5416.80(89)}	761.45(15)	0.08	6178.33(90)
{5395.80(37)}	785.13(6)	0.08	6181.01(37)
5383.16(10)	796.14(7)	0.08	6179.38(12)
5360.33(12)	819.22(1)	0.08	6179.63(16)
5353.25(11)	826.09(4)	0.08	6179.42(12)
{5323.31(37)}	854.97(14)	0.08	6178.36(40)
5317.03(9)	863.37(7)	0.08	6181.48(11)

The arithmetic mean of all calculated $S_{n,i}$ was 6179.45(30) keV. Both results exhibit good agreement with one another and with other works as demonstrated in Table 11.

Table 11. Summary of S_n measurements.

S_n [keV]	Reference
6179.55(24)	This Work ($E_{L-lit.}$)
6179.45(30)	This Work ($E_{L-exp.}$)
6179.5(30)	R. G. Lanier [14]
6179.7(7)	C. M. Baglin [2]

4.7 Thermal Neutron-capture Cross Section for $^{185}\text{Re}(n,\gamma)$

Partial gamma ray-production cross sections σ_γ of the thirteen observed direct ground-state transitions were summed according to the prescription of Equation (21) to compute the total radiative thermal neutron-capture cross section σ_0 for $^{185}\text{Re}(n,\gamma)$. The cross sections were corrected for internal conversion, as applicable. The experimental ground-state transitions and their corrected cross sections are listed in Table 12.

Table 12. Partial gamma ray-production cross sections of observed ground-state transitions below E_{crit} . The cross sections reported are corrected for internal conversion. Quantities in parentheses are uncertainties in significant figure format and braces are proposals resulting from this work.

$E_\gamma(\text{GS})$ [keV]	$\sigma_\gamma(\text{GS})$ [b]
59.00(1)	68.31(137)
99.35(1)	2.51(7)
146.27(1)	0.26(4)
210.69(2)	2.37(37)
316.26(4)	1.58(11)

$\sum \sigma_\gamma^{\text{exp}}(\text{GS})$ is evaluated to be 75(5) b and $P(\text{GS})$, obtained from the DICEBOX simulation output, is found to be 0.10(2). The error was propagated by combination in quadrature [8]. The resulting σ_0 was 84(6) b. The σ_0 reported by DICEBOX was also 84(6) b and it was not particularly sensitive to LDM and PSF combination. A comparison with other works is presented in Table 13.

Table 13. Summary of σ_0 measurements.

σ_0 [b]	Reference
84(6)	This Work
114(3)	S. J. Friesenhahn [40]
112(2)	S. F. Mughabghab [38]
100(8)	H. Pomerance [41]
101(20)	L. Seren [42]
116(5)	R. E. Heft[43]

The result is consistent within one standard deviations of Reference [42], within two standard deviations of Reference [41], and within three standard deviations of Reference [43]. The dominant contributor to the experimental depopulation is the 59.00(1)-keV transition. Therefore, it is also the most significant potential source of error in the

calculation. The 59.05(1) keV-level is the first excited state, which further indicates that σ_0 is not significantly sensitive to the E_{crit} setting.

V. Conclusions and Recommendations

5.1 Conclusions of Research

The total radiative thermal neutron-capture cross section σ_0 for $^{185}\text{Re}(n,\gamma)$ was calculated by summing the experimentally measured partial gamma ray-production cross sections σ_γ associated with the ground-state transitions below 323 keV (under which the decay scheme is known) and combining that summation with the statistical contribution to the ground state from the quasi-continuum, calculated using the Monte Carlo statistical-decay code, DICEBOX. The thermal neutron-capture cross section measured in this work is 84(6) b. This result is statistically similar to measurements from previous works. The binding-energy test revealed 54 new primary transitions and 12 new energy levels, in addition to confirming 69 known primaries, thus enhancing the decay scheme. The neutron-separation energy S_n was determined using all observed primary transitions possessing destination levels below 865 keV and it was found to be 6179.45(30) keV. This result is also comparable to measurements contained in previous works and with the adopted S_n of 6179.7(7) keV. Lastly, the DICEBOX simulations provide very preliminary corroboration of the experimentally measured decay scheme below 323 keV. However, a considerable amount of additional modeling work is required in order to provide a comprehensive validation.

5.2 Significance of Research

The results contained in this work are significant in that the identification of the 54 new potential primary transitions is an important addition to the nuclear data libraries,

particularly the Evaluated Gamma Activation File (EGAF) and Evaluated Nuclear Data File (ENDF).

5.3 Recommendations for Future Research

This work was limited by the absence of coincidence data and an inability to measure the angular distribution of gamma-ray emission, which would allow greater certainty in decay-scheme development and enhance our nuclear structure knowledge of the ^{186}Re compound. Additionally, coincidence data would confirm or rule out the new potential primary transitions identified in this work. Therefore, it is recommended that the experiment be repeated with the remaining highly enriched rhenium metal powder at the BRR. Setup modifications should include incorporation of two HPGe detectors in order to collect γ - γ coincidence data and the use of cold neutrons in lieu of thermal neutrons to enhance statistics. The primary objective of the experiment should be to verify the proposed primary transitions, verify tentative J^π assignments, and to search for new transitions that populate the metastable-excited state at 149(7) keV in order to reduce the uncertainty of its position.

Appendix A

ASSAY

Element: Rhenium Symbol: Re Isotope: 185 Series: LD Batch: 134991	SPECTROGRAPHIC ANALYSIS (SSMS)															
	Element: ppm	Element: ppm	Element: ppm	Element: ppm												
	Ag: <1	I: <.6	Rh: <.5	Tc:												
	Al: 2	In: <.6	Ru: <2	Te: <2												
	As: <.4	Ir: <3	S: 8	Th: <1												
ISOTOPIC ANALYSIS <table><tr><td></td><td>Atomic</td><td>Precision</td></tr><tr><td>Isotope</td><td>Percent</td><td>plus/minus</td></tr><tr><td>185</td><td>96.74</td><td>0.01000</td></tr><tr><td>187</td><td>3.26</td><td>0.01000</td></tr></table>		Atomic	Precision	Isotope	Percent	plus/minus	185	96.74	0.01000	187	3.26	0.01000	Au: <3	K: 3	Sb: <3	Ti: <13
		Atomic	Precision													
	Isotope	Percent	plus/minus													
	185	96.74	0.01000													
	187	3.26	0.01000													
	B: .2	Li: <.04	Sc: <.7	Tl: <1												
	Ba: <.9	Mg: <4	Se: <.8	U: <1												
	Be: .07	Mn: .3	Si: 36	V: <.3												
	Bi: <3	Mo: <2	Sn: <7	W: <3												
	Br: <.8	N:	Sr: <.5	Zn: 4												
	C:	Na: <1	Ta: <3	Zr: <.9												
	Ca: 8	Nb: <.5	LANTHANIDES and ACTINIDES													
	Cb: <.5	Ni: 4														
	Cd: <2	O:	Am:	La: <.7												
	Cl: 9	Os: <4	Bk:	Lu: <.9												
	Co: <.3	P: .8	Ce: <.8	Md:												
	Cr: .5	Pa:	Cf:	Nd: <3												
	Cs: <2	Pb: <2	Cm:	Np:												
	Cu: 2	Pd: <2	Dy: <3	Pr: <.7												
	F: <1	Pm:	Er: <2	Pu:												
Fe: 14	Po:	Es:	Sm: <3													
Ga: <.6	Pt: <3	Eu: <1	Tb: <.8													
Ge: <1	Ra:	Fm:	Y: <.4													
Hf: <4	Rb: <2	Gd: <4	Yb: <3													
Hg: <3	Re: M	Ho: <.8	Tm: <3													
The limits quoted above are an expression of the precision of this measurement only. The error is estimated at less than 1% from known sources of systematic errors.																
Internal Use Only																
Date Entered: 09/06/1995																
Last Change: 04/19/2004 10:39:35 AM																
By: E1H																

* Symbols: M - major; T - trace; I - interference; < - less than; <= less than/equal to; ~ approximately; nd - not detected.

* Request No. 10061; Notebook No. A-107329-L, pgs. 47-49; 57-58; special work authorization numbers 81791, 23880.

* <- No spectrum line visible. Probably absent, definitely less than value given.

* <T- Present but less than value given.

* The spectrographic results reported herein are semi-quantitative estimates and should not be interpreted or construed to be precise quantitative determinations.

Appendix B

186RE 185RE(N,G) E=THERMAL: {~EGAF}

186RE c Evaluated Gamma-ray Activation File (EGAF).

186RE2c Evaluated by A.G. Lerch (AFIT), November 2013.

186RE c BR\$|s{-0}=112 2 (1984MuZY)

186RE cG RI\$Elemental |s(|g) assuming %Abundance=37.4 2

186RE N 2.6738 14 2.673814

186RE PN

C

C

186RE2PN Thermal cross section in barns.

186RE cN NR\$Isotopic |s(|g)=NR*RI.

186RE2cN Divide by |s{-0} for intensity per neutron capture.

186RE L 0 -1

186RE L 59.05 1 (2)-

186RE G 59.00 1 13.29 94 4.14 6

186RE L 99.35 1 (3)- 25.5 NS 25

186RE G 40.35 1 2.35 19 15.6 12

186RE G 99.36 4 0.48 5 4.23 6

186RE L 146.23 1 (3)-

186RE G 46.72 15 0.05 3 8.23 14

186RE G 87.23 1 1.66 11 7.65 11

186RE G 146.27 1 0.13 3 0.96 1

186RE L 173.92 1 (4)-

186RE G 74.56 2 0.88 5 12.0 2

186RE L 186 (6)-

186RE L 210.65 1 (2)- 0.2 NS LT

186RE G 64.42 4 0.03 1 15 12

186RE G 111.34 1 0.64 13 3.80 6

186RE G 151.48 5 1.28 8 1.2 4

186RE G 210.69 2 1.50 24 0.62 3

186RE L 268.78 1 (4)-

186RE G 122.53 1 1.20 32 2.4 6

186RE G 169.43 3 0.24 3 0.78 1

186RE G 209.82 2 0.24 8 0.272 4

186RE L 273.62 1 (4)-

186RE G 99.70 1 0.21 8 4.8 6

186RE G 127.30 4 0.53 11 1.84 23

186RE G 174.27 1 0.78 21 0.74 12

186RE L 313.84 1 (3)+ 24.1 NS 11

186RE G 103.55 3 0.45 3 0.35 1

186RE	G	167.74	1	0.19	5		0.10	0
186RE	G	214.62	2	2.41	48		0.05	0
186RE	G	255.00	2	0.78	32		0.04	0
186RE	L	316.37	2 (1)-			0.20 NS 10		
186RE	G	257.45	5	0.86	13		0.31	4
186RE	G	316.26	4	1.31	8		0.21	0
186RE	L	317.82	1 (5)-					
186RE	G	143.92	1	1.15	24		1.25	14
186RE	G	218.94	21	0.05	3		0.24	1
186RE	L	322.32	1 (3)-					
186RE	G	111.67	1	0.67	19		3.3	6
186RE	G	148.37	1	0.04	1		1.3	4
186RE	G	176.11	8	0.17	5		0.8	3
186RE	G	223.03	3	0.23	8		0.38	4
186RE	G	263.33	20	0.11	3		0.24	11
186RE	L	330	(5)+			17.3 NS 6		
186RE	G	144.15	1	2.51	56		0.15	0
186RE	L	351.06	2 (3)+			0.2 NS LT		
186RE	G	204.96	15	0.05	3		0.06	0
186RE	G	251.81	3	4.63	27		0.04	0
186RE	L	378.35	2 (2)-					
186RE	G	61.93	4	1.15	19		17.8	3
186RE	G	232.10	2	0.56	8		0.48	1
186RE	G	319.40	4	0.40	3		0.14	7
186RE	G	378.42	5	1.58	11		0.13	0
186RE	L	417.77	1 (5)-					
186RE	G	144.15	1	0.32	11		1.4	4
186RE	G	148.99	1	0.32	11		1.2	16
186RE	G	271.59	12	0.13	3		0.12	0
186RE	L	420.39	4 (4)+					
186RE	G	106.55	4	0.53	5		3.5	3
186RE	L	425.56	4 (2+,3+,4+)					
186RE	G	111.81	4	0.16	6			
186RE	G	425.83	7	0.16	3			
186RE	L	462.93	2 (5)-					
186RE	G	145.13	1	0.13	3		1.4	4
186RE	G	189.25	2	0.94	5		0.62	23
186RE	G	193.95	10	0.11	3		0.59	23
186RE	G	289.44	20	0.08	1		0.18	9
186RE	G	363.45	5	0.45	11		0.05	1
186RE	L	469.74	1 (4)-					
186RE	G	147.42	1	1.47	29		1.3	4

186RE	G	201.00	3	0.24	3	0.51	20
186RE	G	295.88	15	0.19	5	0.25	1
186RE	L	470.50	2 (3)-				
186RE	G	92.15	1	0.48	3	6.01	9
186RE	G	148.09	6	0.03	1	1.3	4
186RE	G	201.78	10	0.03	1	0.71	10
186RE	G	411.18	20	0.27	5		
186RE	L	471	(4)+				
186RE	G	141.27	3	0.32	5	1.6	3
186RE	L	497.29	4 (6-)				
186RE	G	179.45	4	0.21	3	0.75	17
186RE	L	500.57	1 (4)+				
186RE	G	149.52	1	0.88	40	1.06	11
186RE	G	401.21	1	0.11	3		
186RE	L	534.39	4 (4)-				
186RE	G	260.87	15	0.32	5	0.24	11
186RE	G	360.44	4	1.02	5	0.14	0
186RE	L	548.98	6 (+)				
186RE	G	123.42	4	0.29	3	2.27	4
186RE	L	559.78	4 (5)+				
186RE	G	134.22	1	0.08	1		
186RE	G	139.42	1	0.19	3	1.35	19
186RE	L	562	(6+)				
186RE	G	232.05	4	0.78	5	0.48	1
186RE	L	577.65	2 (2-)				
186RE	G	199.27	3	0.37	3	0.53	21
186RE	G	261.37	5	0.91	19	0.35	1
186RE	L	588.67	3 (4-)				
186RE	G	118.18	2	0.43	3	2.7	6
186RE	L	601.65	4 (1)+				
186RE	G	285.16	4	0.53	3	0.03	0
186RE	G	390.93	5	3.40	24	0.01	0
186RE	L	623.83	6 (1-)				
186RE	G	301.36	15	0.16	3	0.93	1
186RE	G	413.21	6	0.45	3		
186RE	L	646.13	6 (5-)				
186RE	G	176.35	6	0.64	11	0.8	3
186RE	G	228.42	10	0.21	5	0.35	15
186RE	G	328.42	20	0.13	3	0.13	6
186RE	L	657.96	4 (2)+				
186RE	G	56.41	1	0.13	3	29.7	5
186RE	G	335.67	13	0.05	1	0.02	0

186RE	G	341.38	20	0.13	5	0.02	0
186RE	L	665.11	4	(5)+			
186RE	G	164.54	3	0.27	3	0.89	7
186RE	L	680.00	5	(2-,3-)			
186RE	G	357.68	5	0.32	3		
186RE	G	469.39	20	0.32	11		
186RE	G	680.00	10	0.40	11		
186RE	L	685.99	2	(3-)			
186RE	G	108.34	1	0.19	8	3.6	6
186RE	G	215.28	15	0.11	5	0.42	7
186RE	G	307.66	4	0.75	8	0.22	0
186RE	L	689.3		(1-)			
186RE	L	691.38	6	(6-)			
186RE	G	193.95	10	0.08	3	0.57	22
186RE	G	228.42	10	0.08	3	0.35	15
186RE	G	373.63	7	0.08	1	0.09	5
186RE	L	736.07	4	(5-)			
186RE	G	147.40	2	1.18	8	1.3	4
186RE	L	744.68	14	(3)+			
186RE	G	86.45	24				
186RE	G	744.50	46	0.19	8		
186RE	L	753.57	25				
186RE	L	761.45	15	(1-,2,3-)			
186RE	G	438.91	21	0.16	3		
186RE	G	551.30	26	0.40	5		
186RE	G	760.88	38	0.24	3		
186RE	L	785.13	6				
186RE	G	406.77	6	0.21	3		
186RE	G	469.42	22	0.19	5		
186RE	G	785.09	39	0.08	3		
186RE	L	791.34	16	(1-)			
186RE	L	796.14	7	(LE 3)			
186RE	G	218.27	10	0.11	1		
186RE	G	418.30	19	0.29	3		
186RE	G	479.70	22	0.88	8		
186RE	G	584.34	31	0.48	5		
186RE	G	796.22	46	0.16	8		
186RE	L	803	10				
186RE	L	812.20		(1-)			
186RE	L	819.22	10	(2-,3-)			
186RE	G	496.94	25	0.35	8		
186RE	G	607.58	29	0.64	8		

186RE	G	645.72	31	0.35	5		
186RE	G	760.88	38	0.24	3		
186RE	G	819.95	42	0.08	3		
186RE	L	821.34	5	(LE 3)			
186RE	G	163.31	6	0.08	3		
186RE	G	219.83	5	0.16	1		
186RE	L	826.09	4	(4-)			
186RE	G	140.07	3	0.67	11	1.5	5
186RE	G	237.60	15	0.11	3	0.32	14
186RE	G	355.63	5	0.29	3	0.10	5
186RE	L	854.97	14	(4+)			
186RE	G	110.24	9	0.37	5	3.4	6
186RE	G	196.90	17	0.05	1	0.34	1
186RE	L	857.9		(2-,3-)			
186RE	L	863.37	7	(2-,3-)			
186RE	G	286.41	8	0.13	1		
186RE	L	872.64	11	(-)			
186RE	L	879.3		(2-,3-)			
186RE	L	888.4		(4-)			
186RE	L	889.8		(1-,2-,3-)			
186RE	L	895.08	10	(2-,3-,4-)			
186RE	L	902.37	9	(2-,3-)			
186RE	L	913.6		(2-,3-)			
186RE	L	923.58	19	(2-,3-)			
186RE	L	930		(-)			
186RE	L	935.37	19	(2-,3-)			
186RE	L	938.3		(1-)			
186RE	L	947.6	6	(2-,3-)			
186RE	L	954.68	15				
186RE	L	972.81	14	(-)			
186RE	L	989.04	14	(2-,3-)			
186RE	L	997.84		(5+)			
186RE	L	999.4	4	(2-,3-,4-)			
186RE	L	1003.06	9	(2-,3-,4-)			
186RE	L	1015.0		(2-,3-,4-)			
186RE	L	1019.4		(1-,2-,4-)			
186RE	L	1040.24	11	(2-,3-,4-)			
186RE	L	1042.9		(1-)			
186RE	L	1046.9		(2-,3-,4-)			
186RE	L	1053.4		(1-,2-,3-)			
186RE	L	1057.1		(2-,3-)			
186RE	L	1068.5	3	(2-,3-)			

186RE	L	1073.3		(2-,3-)
186RE	L	1097.14	9	(4-)
186RE	L	1102.81	10	(2-,3-)
186RE	L	1122.62	18	(2-,3-)
186RE	L	1132.19	13	
186RE	L	1140.89	22	(2-,3-)
186RE	L	1151.25	9	(4-)
186RE	L	1157.92	13	(2-,3-,4-)
186RE	L	1163.0		(1-)
186RE	L	1172.08	8	(-)
186RE	L	1184.87	11	(2-,3-)
186RE	L	1194.3		(2-,3-,4-)
186RE	L	1197.78	8	(2-,3-)
186RE	L	1219.1		(1-)
186RE	L	1227.87	15	(1-,2-,3-)
186RE	L	1232.0		(2-,3-)
186RE	L	1242.69	14	(2-,3-)
186RE	L	1249.09	18	(-)
186RE	L	1263.95	10	(1-)
186RE	L	1268.13	11	(2-,3-,4-)
186RE	L	1275.3		(1-,2-,3-)
186RE	L	1286.00	24	(2-,3-)
186RE	L	1297.5		(1-,2-,3-)
186RE	L	1307.47	13	(-)
186RE	L	1317.43	11	(2-,3-,4-)
186RE	L	1322.05	11	(2-,3-)
186RE	L	1351.12	14	(4-)
186RE	L	1355.4	3	(2-,3-)
186RE	L	1360.2	4	(2-,3-,4-)
186RE	L	1370.8	3	
186RE	L	1375.1		(1-,2-,3-)
186RE	L	1386.21	13	(2-,3-)
186RE	L	1392.7		(2-,3-)
186RE	L	1398.8		(1-,2-,3-)
186RE	L	1403.2		(1-)
186RE	L	1405.52	8	(2-,3-,4-)
186RE	L	1419.0	3	(2-,3-)
186RE	L	1424.5		(2-,3-)
186RE	L	1431.0		(4-)
186RE	L	1437.94	19	
186RE	L	1449.1	3	(1-,2-,3-)
186RE	L	1457.40	15	(2-,3-)

186RE	L	1462.1	4	(2-,3-)
186RE	L	1475.29	22	
186RE	L	1477.53	7	(-)
186RE	L	1486.64	10	
186RE	L	1517.15	21	
186RE	L	1524.97	13	(4-)
186RE	L	1532.50	23	(2-,3-)
186RE	L	1539.6	7	(1-,2-,3-)
186RE	L	1544.69	8	(-)
186RE	L	1550.33	13	(1-,2-,3-)
186RE	L	1566.38	21	(2-,3-,4-)
186RE	L	1572.09	14	(1-,2-,3-)
186RE	L	1577.0	3	(2-,3-,4-)
186RE	L	1587.12	9	
186RE	L	1592.91	14	(2-,3-)
186RE	L	1606.4	3	
186RE	L	1627.89	13	(2-,3-,4-)
186RE	L	1635.80	19	
186RE	L	1644.93	19	(1-,2-,3-)
186RE	L	1647.61	18	(2-,3-,4-)
186RE	L	1659.7	7	(-)
186RE	L	1665.8	3	(2-,3-,4-)
186RE	L	1672.13	11	(1-,2-,3-)
186RE	L	1677.36	12	
186RE	L	1683.39	11	(2-,3-,4-)
186RE	L	1700.41	14	(2-,3-)
186RE	L	1712.1	5	(2-,3-)
186RE	L	1719.43	10	
186RE	L	1722.66	11	(2-,3-
186RE	L	1742.85	14	
186RE	L	1757.14	24	(2-,3-)
186RE	L	1767.09	11	
186RE	L	1791.50	21	(-)
186RE	L	1795.49	13	
186RE	L	1816.0	6	(2-,3-,4-)
186RE	L	1826.64	18	(2-,3-,4-)
186RE	L	1839.7	4	(1-,2-,3-)
186RE	L	1845.3	5	(2-,3-)
186RE	L	1881.19	14	
186RE	L	1888.81	14	
186RE	L	1906.0	4	
186RE	L	1913.27	16	

186RE	L	1963.9	6		
186RE	L	1982.2	3		
186RE	L	1991.4	3		
186RE	L	2000.06	14		
186RE	L	2055.0	8		
186RE	L	2060.00	9		
186RE	L	2082.32	20		
186RE	L	2103.89	11		
186RE	L	2141.19	6		
186RE	L	2203.20	24		
186RE	L	2218.94	23		
186RE	L	2244.59	13		
186RE	L	2252.30	25		
186RE	L	2261.6	4		
186RE	L	2267.58	38		
186RE	L	6179.60	3	(2+,3+)	
186RE	G	3917.96	38	0.027	5
186RE	G	3927.26	24	0.032	5
186RE	G	3934.97	12	0.115	11
186RE	G	3960.62	17	0.064	13
186RE	G	3976.36	23	0.051	8
186RE	G	4038.37	5	0.016	5
186RE	G	4075.67	10	0.131	11
186RE	G	4097.23	19	0.064	5
186RE	G	4119.55	8	0.155	11
186RE	G	4124.58	74	0.011	5
186RE	G	4179.49	13	0.214	3
186RE	G	4188.17	26	0.032	5
186RE	G	4197.40	26	0.035	5
186RE	G	4215.69	53	0.083	32
186RE	G	4266.28	15	0.104	11
186RE	G	4273.57	39	0.040	5
186RE	G	4290.74	21	0.037	5
186RE	G	4298.36	13	0.128	13
186RE	G	4334.20	52	0.053	16
186RE	G	4339.82	40	0.043	11
186RE	G	4352.91	17	0.096	13
186RE	G	4363.57	60	0.029	5
186RE	G	4384.06	12	0.053	5
186RE	G	4388.05	20	0.035	3
186RE	G	4412.46	10	0.118	11
186RE	G	4422.41	23	0.080	8

186RE	G	4436.70	13	0.080	8
186RE	G	4456.89	10	0.163	11
186RE	G	4460.12	9	0.182	13
186RE	G	4467.47	43	0.019	3
186RE	G	4479.14	13	0.067	5
186RE	G	4496.15	10	0.091	8
186RE	G	4502.18	11	0.080	5
186RE	G	4507.41	10	0.166	13
186RE	G	4513.79	28	0.075	8
186RE	G	4519.89	37	0.051	11
186RE	G	4531.93	17	0.075	8
186RE	G	4534.61	18	0.083	8
186RE	G	4551.65	12	0.059	5
186RE	G	4573.16	28	0.070	13
186RE	G	4586.63	13	0.053	5
186RE	G	4592.42	8	0.144	11
186RE	G	4602.58	27	0.048	16
186RE	G	4607.45	13	0.091	16
186RE	G	4613.16	20	0.131	19
186RE	G	4629.21	12	0.078	5
186RE	G	4634.85	7	0.257	19
186RE	G	4639.98	69	0.011	3
186RE	G	4647.04	22	0.027	3
186RE	G	4654.57	12	0.051	5
186RE	G	4662.39	20	0.080	11
186RE	G	4692.90	9	0.126	13
186RE	G	4702.01	6	0.029	8
186RE	G	4704.25	21	0.061	5
186RE	G	4717.42	32	0.019	5
186RE	G	4722.14	14	0.061	8
186RE	G	4729.46	28	0.029	3
186RE	G	4741.60	18	0.080	8
186RE	G	4760.54	28	0.043	5
186RE	G	4774.02	7	0.612	43
186RE	G	4793.33	12	0.083	8
186RE	G	4808.72	28	0.061	1
186RE	G	4819.29	38	0.027	8
186RE	G	4824.14	30	0.043	8
186RE	G	4828.42	13	0.102	13
186RE	G	4857.49	10	0.227	19
186RE	G	4862.11	10	0.607	43
186RE	G	4872.06	12	0.184	13

186RE	G	4893.53	23	0.043	5
186RE	G	4911.40	10	0.043	5
186RE	G	4915.58	9	0.144	11
186RE	G	4930.44	17	0.043	5
186RE	G	4936.84	13	0.278	29
186RE	G	4951.66	14	0.110	11
186RE	G	4981.75	7	0.270	19
186RE	G	4994.66	10	0.102	8
186RE	G	5007.45	7	0.743	51
186RE	G	5021.61	12	0.083	8
186RE	G	5028.28	8	0.714	51
186RE	G	5038.64	21	0.024	3
186RE	G	5047.34	12	0.086	8
186RE	G	5056.91	17	0.070	8
186RE	G	5076.72	9	0.217	16
186RE	G	5082.39	8	0.144	11
186RE	G	5111.01	26	0.128	13
186RE	G	5139.29	10	0.628	45
186RE	G	5176.47	8	0.414	29
186RE	G	5180.08	39	0.032	5
186RE	G	5190.49	13	0.037	5
186RE	G	5206.72	13	0.168	16
186RE	G	5224.84	14	0.037	5
186RE	G	5231.92	60	0.008	3
186RE	G	5244.15	18	0.104	11
186RE	G	5255.94	18	0.254	3
186RE	G	5277.15	8	0.390	27
186RE	G	5284.44	9	0.195	13
186RE	G	5306.88	10	1.134	8
186RE	G	5317.03	9	0.123	11
186RE	G	5323.31	37	0.013	3
186RE	G	5353.25	11	0.390	27
186RE	G	5360.33	12	0.179	13
186RE	G	5383.16	10	0.070	5
186RE	G	5388.18	15	0.032	3
186RE	G	5395.80	37	0.021	3
186RE	G	5416.80	89	0.008	3
186RE	G	5425.95	24	0.003	3
186RE	G	5493.41	8	0.246	19
186RE	G	5601.63	10	0.305	21
186RE	G	5619.06	99	0.003	3
186RE	G	5644.96	11	0.214	16

186RE	G	5678.68	30	0.011	3
186RE	G	5709.56	11	0.321	24
186RE	G	5754.52	7	0.011	3
186RE	G	5759.25	41	0.005	3
186RE	G	5800.81	12	0.043	3
186RE	G	5857.03	9	0.385	27
186RE	G	5862.55	42	0.024	5
186RE	G	5905.44	20	0.051	11
186RE	G	5910.60	8	1.658	112
186RE	G	5968.79	16	0.043	3
186RE	G	6005.45	12	0.152	11
186RE	G	6032.87	13	0.166	16
186RE	G	6080.14	8	0.337	24
186RE	G	6120.51	8	0.329	21
186RE	G	6179.22	15	0.051	3

Bibliography

- [1] D. W. Seegmiller, M. Lindner and R. A. Meyer, "Re-186: Nuclear Structure and an Isomer of Half-life 200,000 y," *Nuc. Phys. A*, vol. 185, pp. 94-112, 1972.
- [2] *Evaluated Nuclear Structure Data File (ENSDF)*, an electronic database of evaluated experimental nuclear structure data maintained by the National Nuclear Data Center, Brookhaven National Laboratory, URL <http://www.nndc.bnl.gov/ensdf/>.
- [3] Defense Science Board, "Radionuclide Power to Lighten the Soldiers' Load," *Technology and Innovation Enablers for Superiority in 2030*, pp. 48-54, 2013.
- [4] P. M. Walker and J. J. Carroll, "Ups and Downs of Nuclear Isomers," *Physics Today*, pp. 39-44, June 2005.
- [5] J. J. Carroll, M. S. Litz, K. A. Netherton, S. L. Henriquez and N. R. Pereira, "Nuclear structure and depletion of nuclear isomers using electron linacs," in *AIP Conf. Proc.* 1525, 586, 2013.
- [6] M. Krtička, R. B. Firestone, D. P. McNabb, B. W. Sleaford, U. Agvaanluvsan, T. Belgia and Z. Révay, "Thermal neutron capture cross sections of the palladium isotopes," *Phys. Rev. C*, vol. 77, 054615, 2008.
- [7] Z. Révay and T. Belgia, "Principles of the PGAA method," in *Handbook of Prompt Gamma Activation Analysis with Neutron Beams*, G. L. Molnár, Ed., Dordrecht, Kluwer Academic Publishers, 2004, pp. 1-28.
- [8] G. F. Knoll, *Radiation Detection and Measurement*, 4, Ed., Hoboken, New Jersey: Wiley, 2010.

- [9] Z. Revay, R. B. Firestone, T. Belgya and M. G., "Prompt Gamma-Ray Spectrum Catalog," in *Handbook of Prompt Gamma Activation Analysis with Neutron Beams*, G. L. Molnar, Ed., Dordrecht, Kluwe Academic Publishers, 2004, pp. 173-364.
- [10] J. J. Carroll, Private communication.
- [11] A. Bohr and B. R. Mottelson, "Some Current Themes in Nuclear Research," *Physica Scripta*, vol. 10A, pp. 13-20, 1974.
- [12] K. S. Krane, *Introductory Nuclear Physics*, New Jersey: Wiley, 1988.
- [13] C. Wheldon, N. I. Ashwood, N. Curtis, M. Freer, T. Munoz-Britton, V. A. Ziman, T. Faestermann, H. Wirth, R. Hertenberger, R. Lutter, R. Gernhauser, R. Krucken and L. Maier, "High-resolution particle spectroscopy of ^{186}Re ," *Journ. of Phys. G*, vol. 36, pp. 1-11, 2009.
- [14] R. G. Lanier, R. K. Sheline, H. F. Mahlein, T. von Egidy, W. Kaiser, H. R. Koch, U. Gruber, B. P. K. Maier, O. W. B. Schult, D. W. Hafemeister and E. B. Shera, "Nuclear Levels in Re-186," *Phys. Rev.*, vol. 178, pp. 1919-1948, 1969.
- [15] L. Zanini, Ph.D. thesis, University of Torino, 1998.
- [16] C. J. Bridgman, *Introduction to the Physics of Nuclear Explosives*, Fort Belvoir, VA: Defense Threat Reduction Agency, 2001.
- [17] *Evaluated Nuclear Data File (ENDF) Retrieval and Plotting*, an electronic database of evaluated experimental nuclear data maintained by the National Nuclear Data Center, Brookhaven National Laboratory, URL <http://www.nndc.bnl.gov/sigma/>.
- [18] M. Krtička, Ph.D. thesis, Charles University in Prague, 2002.
- [19] N. Bohr, "Neutron Capture and Nuclear Constitution," *Nature (London)*, vol. 137, no. 3461, pp. 344-348, 1936.

- [20] A. M. Hurst, R. B. Firestone, B. W. Sleaford, N. C. Summers, Z. Révay, L. Szentmiklósi, M. S. Basunia, T. Belgia, J. E. Escher and M. Krtička, "A structural evaluation of the tungsten isotopes via thermal neutron capture," *Phys. Rev. C*, vol. 89, 014606, 2014.
- [21] C. E. Porter and R. G. Thomas, "Fluctuations of Nuclear Reaction Widths," *Phys. Rev.*, vol. 104, no. 2, p. 483, 1956.
- [22] S. Hilaire, "Level Densities," in *Workshop on Nuclear Data and Nuclear Reactors: Physics, Design, Safety*, Trieste, 2000.
- [23] T. von Egidy and D. Bucurescu, "Systematics of nuclear level density parameters," *Phys. Rev. C*, vol. 72, no. 4, 044311, 2005.
- [24] T. von Egidy, H. H. Schmidt and A. N. Behkami, "Nuclear Level Densities and Spacing Distributions: Part II," *Nuc. Phys. A*, vol. 481, no. 2, pp. 189-206, 1988.
- [25] S. I. Al-Quraishi, S. M. Grimes, T. N. Massey and D. A. Resler, "Level densities for $20 < A < 110$," *Phys. Rev. C*, vol. 67, 015803, 2003.
- [26] F. Bečvář, "Photon Strength Function Phenomenology: Achievements and open problems," Charles University, Prague, 2008.
- [27] J. Kopecky and M. Uhl, "Test of gamma-ray strength functions in nuclear reaction model calculations," *Phys. Rev. C*, vol. 41, 1941, 1990.
- [28] R. M. Lindstrom and Z. Révay, "Beams and Facilities," in *Handbook of Prompt Gamma Activation Analysis with Neutron Beams*, G. L. Molnár, Ed., Dordrecht, Kluwer Academic Publishers, 2004, pp. 31-58.
- [29] H. D. Choi, "Characteristics of PGAA Facilities," in *Database of Prompt Gamma Rays from Slow Neutron Capture*, Viena, International Atomic Energy Agency, 2007, pp. 21-40.
- [30] G. F. Knoll, *Radiation Detection and Measurement*, 4th ed., New Jersey: Wiley, 2010.
- [31] A. M. Hurst, Private communication.

- [32] L. Szentmiklósi, Private communication.
- [33] Z. Révay and G. L. Molnár, "Standardisation of the prompt gamma activation analysis method," *Radiochim. Acta*, vol. 91, no. 6, pp. 361-369, 2003.
- [34] *Chart of Nuclides*, an electronic database of basic properties of atomic nuclei maintained by the National Nuclear Data Center, Brookhaven National Laboratory, URL <http://www.nndc.bnl.gov/chart/>.
- [35] *BrIcc v2.3S Conversion Coefficient Calculator*, an electronic calculator maintained by the Australian National University, URL <http://bricc.anu.edu.au/>.
- [36] Z. Révay, T. Belgya and G. L. Molnár, "Application of Hypermet-PC in PGAA," *Journ. Radioanal. Nucl. Chem*, vol. 265, no. 2, pp. 261-265, 2005.
- [37] S. S. Dietrich and B. L. Berman, "Atlas of photoneutron cross sections obtained with monoenergetic photons," *Atomic Data and Nuclear Data Tables*, vol. 38, no. 2, pp. 199-338, 1988.
- [38] S. F. Mughabghab, *Atlas of Neutron Resonances: Resonance Parameters and Thermal Cross Sections for Z=1-100*, 5th ed., Amsterdam: Elsevier, 2006.
- [39] F. Bečvář, Y. Honzatko, M. Králík, D. N. Nguen, T. Stadnikov and S. A. Telezhnikov, "Study of the reaction $\text{Re-185}(n,\gamma)\text{Re-186}$ in isolated resonances," *Sov. J. Nucl. Phys.*, vol. 37, no. 6, pp. 809-814, 1983.
- [40] S. J. Friesenhahn, D. A. Gibbs, E. Haddad, F. H. Frohner and W. M. Lopez, "Neutron capture cross sections and resonance parameters of rhenium from 0.01 eV to 30 keV," *Journ. of Nuc. Energy*, vol. 22, p. 191, 1968.
- [41] H. Pomerance, "Thermal neutron capture cross sections," *Phys. Rev.*, vol. 88, p. 412, 1952.
- [42] L. Seren, H. N. Friedlander and S. H. Turkel, "Thermal neutron activation cross sections," *Phys. Rev.*, vol. 72, p. 888, 1947.

- [43] R. E. Heft, "A consistent set of nuclear-parameter values for absolute instrumental neutron activation analysis," in *Conf. on Computers in Activ. Analysis*, Mayaguez, 1978.

Vita

Captain Andrew G. Lerch attended the United States Military Academy at West Point, New York, graduating in 2005 with a Bachelor of Science degree in Nuclear Engineering and a commission as a Second Lieutenant of Armor in the U.S. Army. His first assignment was at Fort Knox, Kentucky as a student in the Armor Officer Basic Course. In February 2006, he was assigned to 1st Battalion, 15th Infantry Regiment, 3rd Heavy Brigade Combat Team, 3rd Infantry Division at Fort Benning, Georgia. Over the course of five years with the Battalion, Captain Lerch served as the Assistant Battalion S1, the Battalion S1, a tank platoon leader, the Battalion S4, and the Battalion Rear Detachment Commander. While serving as a tank platoon leader, he deployed to Iraq in support of OPERATION IRAQI FREEDOM from March 2007 to May 2008. In March 2010, while remaining at Fort Benning, he attended and successfully completed the Maneuver Captains Career Course. During this time, Captain Lerch transitioned from an Armor officer to a Nuclear & Counterproliferation officer. He then entered the Graduate School of Engineering and Management, Air Force Institute of Technology in June 2012 in pursuance of a Master of Science degree in Nuclear Engineering. Captain Lerch was selected for promotion to Major by the Fiscal Year 2013 Selection Board. Following graduation, he will be assigned to the Nuclear Technologies Department within the Defense Threat Reduction Agency's Research and Development Directorate.

REPORT DOCUMENTATION PAGE				Form Approved OMB No. 074-0188	
<p>The public reporting burden for this collection of information is estimated to average 1 hour per response, including the time for reviewing instructions, searching existing data sources, gathering and maintaining the data needed, and completing and reviewing the collection of information. Send comments regarding this burden estimate or any other aspect of the collection of information, including suggestions for reducing this burden to Department of Defense, Washington Headquarters Services, Directorate for Information Operations and Reports (0704-0188), 1215 Jefferson Davis Highway, Suite 1204, Arlington, VA 22202-4302. Respondents should be aware that notwithstanding any other provision of law, no person shall be subject to any penalty for failing to comply with a collection of information if it does not display a currently valid OMB control number.</p> <p>PLEASE DO NOT RETURN YOUR FORM TO THE ABOVE ADDRESS.</p>					
1. REPORT DATE (DD-MM-YYYY) 27 Mar 2014		2. REPORT TYPE Master's Thesis		3. DATES COVERED (From - To) Jun 2012 - Mar 2014	
4. TITLE AND SUBTITLE Nuclear Structure of Rhenium-186 Revealed by Neutron-capture Gamma Rays				5a. CONTRACT NUMBER	
				5b. GRANT NUMBER	
				5c. PROGRAM ELEMENT NUMBER	
6. AUTHOR(S) Lerch, Andrew G., CPT, USA				5d. PROJECT NUMBER 13P318	
				5e. TASK NUMBER	
				5f. WORK UNIT NUMBER	
7. PERFORMING ORGANIZATION NAMES(S) AND ADDRESS(S) Air Force Institute of Technology Graduate School of Engineering and Management (AFIT/EN) 2950 Hobson Way, Building 640 Wright-Patterson AFB, OH 45433-7765				8. PERFORMING ORGANIZATION REPORT NUMBER AFIT-ENP-14M-21	
9. SPONSORING/MONITORING AGENCY NAME(S) AND ADDRESS(ES) Defense Threat Reduction Agency 8725 John J. Kingman Rd Stop 6201 Fort Belvoir, VA 22060-6201 (703) 767-5870 dtra.publicaffairs@dtra.mil				10. SPONSOR/MONITOR'S ACRONYM(S) DTRA OP/CSU	
				11. SPONSOR/MONITOR'S REPORT NUMBER(S)	
12. DISTRIBUTION/AVAILABILITY STATEMENT Distribution Statement A. Approved for Public Release; Distribution Unlimited					
13. SUPPLEMENTARY NOTES This material is declared a work of the U.S. Government and is not subject to copyright protection in the United States.					
<p>The total radiative thermal neutron-capture cross section of $^{185}\text{Re}(n,\gamma)$ was calculated from measurements of its gamma-ray spectrum following irradiation of a highly enriched ^{185}Re target in the guided thermal-neutron beam at the Budapest Research Reactor. The cross section was obtained by first summing the experimentally measured partial gamma ray-production cross sections associated with the known ground-state transitions below 323 keV. Combined with the contribution to ground-state population from the quasi-continuum, which was generated by the DICEBOX statistical-decay code, the resulting thermal neutron-capture cross section was determined to be 84(6) b. This result is statistically comparable to previous works. Additionally, 12 levels and 54 primary transitions were newly identified in this work via the binding-energy test, thus improving the decay scheme. All observed primary transitions populating levels below 865 keV were used to perform an independent measurement of the neutron-separation energy, which was found to be 6179.45(30) keV. This result is also consistent with measurements made in previous works and with the adopted neutron-separation energy of 6179.7(7) keV.</p>					
15. SUBJECT TERMS Nuclear Structure, Prompt Gamma Activation Analysis, Rhenium-186, Thermal-Neutron Capture					
16. SECURITY CLASSIFICATION OF:			17. LIMITATION OF ABSTRACT	18. NUMBER OF PAGES	19a. NAME OF RESPONSIBLE PERSON
a. REPORT	b. ABSTRACT	c. THIS PAGE			McHale, Stephen R., LTC, Ph.D, USA
U	U	U	UU	112	19b. TELEPHONE NUMBER (Include area code) (937) 255-6565 x 4438 stephen.mchale@afit.edu